

Chemistry-climate interactions in the Goddard Institute for Space Studies general circulation model

2. New insights into modeling the preindustrial atmosphere

J. Lee Grenfell¹

Stratosphärengruppe, Institut für Meteorologie, Freie Universität Berlin, Berlin, Germany

Drew T. Shindell, Dorothy Koch, and David Rind

NASA Goddard Institute for Space Studies and Center for Climate Research, Columbia University, New York, USA

Abstract. We investigate the chemical (hydroxyl and ozone) and dynamical response to changing from present-day to preindustrial conditions in the Goddard Institute for Space Studies general circulation model. We identify three main improvements not included by many other works. First, our model includes interactive cloud calculations. Second, we reduce sulfate aerosol which impacts NO_x partitioning hence O_x distributions. Third, we reduce sea surface temperatures and increase ocean ice coverage which impact water vapor and ground albedo, respectively. Changing the ocean data (hence water vapor and ozone) produces a potentially important feedback between the Hadley circulation and convective cloud cover. Our present-day run (run 1, control run) global mean OH value was $9.8 \times 10^5 \text{ molecules cm}^{-3}$. For our best estimate of preindustrial conditions run (run 2) which featured modified chemical emissions, sulfate aerosol, and sea surface temperatures/ocean ice, this value changed to $10.2 \times 10^5 \text{ molecules cm}^{-3}$. Reducing only the chemical emissions to preindustrial levels in run 1 (run 3) resulted in this value increasing to $10.6 \times 10^5 \text{ molecules cm}^{-3}$. Reducing the sulfate in run 3 to preindustrial levels (run 4) resulted in a small increase in global mean OH ($10.7 \times 10^5 \text{ molecules cm}^{-3}$). Changing the ocean data in run 4 to preindustrial levels (run 5) led to a reduction in this value to $10.3 \times 10^5 \text{ molecules cm}^{-3}$. Mean tropospheric ozone burdens were 423, 306, 305, 305, and 310 Tg for runs 1–5, respectively.

1. Introduction

Identifying trends in tropospheric ozone (O_3) occurring since the preindustrial (PI) era is made difficult due to insufficient spatial and temporal observations, a relatively short lifetime (of the order weeks in the planetary boundary layer (PBL) to months in the free troposphere), and the fact that this specie is not emitted directly into the atmosphere. Therefore modeling studies are currently the preferred tool for tropospheric trend assessment. In recent years, three-dimensional (3-D) simulations with chemistry have emerged. Of these, estimates of mean ozone increases range from 40% [Roelofs *et al.*, 1997] to 60–70% [Wang and Jacob, 1998; Lelieveld and Van Dorland, 1995]. Changes in hydroxyl (OH) are more uncertain, being subject to the opposing effects of increasing CO and CH_4 (which directly lower OH) and increasing O_x ($=\text{O}^3\text{P} + \text{O}^1\text{D} + \text{O}_3$) and NO_x (which increase OH via $j\text{O}_3 \rightarrow \text{O}^1\text{D} + \text{H}_2\text{O} \rightarrow 2\text{OH}$ and $\text{HO}_2 + \text{NO} \rightarrow \text{OH} + \text{NO}_2$, respectively). Estimates are in the following range: 17% decrease [Brasseur *et al.*, 1998] to a 6% increase [Bernsten *et al.*, 1997] in mean OH concen-

tration since the PI era. These, and additional studies, also report radiative changes due to O_x increases. Moving from clear-sky to cloudy conditions tends to lower the global mean forcing value by 20–60% [Haywood *et al.*, 1998; Forster *et al.*, 1996]. However, the above, and other general circulation model studies with chemistry [Chalita *et al.*, 1996; Bernsten *et al.*, 1997; Van Dorland *et al.*, 1997; Levy *et al.*, 1997], adopted climatological cloud cover when calculating tropospheric O_x increase. In this study we include an on-line, prognostic calculation of clouds. We also investigate the chemical effect of reducing the sulfate aerosol distribution. Finally, we investigate the effect of changing our fixed monthly climatological mean sea surface temperatures (SSTs) and ocean ice distribution from present day (PD) to PI.

We employ a 3-D model, the Goddard Institute for Space Studies (GISS) general circulation model (GCM), in order to gain new insight into anthropogenically driven oxidative and radiative changes to the troposphere from PD to PI conditions. In summary, compared with the PD control run, we have modified the following to PI conditions: (1) chemical emissions, including the ozone precursors, (2) the sulfate aerosol distribution, (3) the oceanographic data, and (4) the greenhouse gases (GHGs). We report resulting changes to the tropospheric hydroxyl (OH), O_x ($=\text{O}_3 + \text{O}^1\text{D} + \text{O}^3\text{P}$), and water vapor concentrations as well as the associated dynamical/cloud response. Section 2 provides a model description and overview

¹Formerly at NASA Goddard Institute for Space Studies and Center for Climate Research, Columbia University, New York, USA.

Copyright 2001 by the American Geophysical Union.

Paper number 2000JD000090.
0148-0227/01/2000JD000090\$09.00

Table 1. Overview of Runs

Run 1	Run 2	Run 3	Run 4	Run 5
PD conditions	PI emissions, sulfate aerosol, ocean data, and greenhouse gases	PI emissions, PD sulfate aerosol, ocean data, and greenhouse gases	run 3 but with PI sulfate aerosol	run 4 but with PI ocean data
Control run	best estimate of PI conditions	most comparable to other works	test effect of sulfate	test effect of ocean

of the runs; section 3 discusses results; section 4 presents conclusions and future work.

2. Model Description

The GISS II' (two prime) GCM [Hansen *et al.*, 1997] was developed from the GISS GCM version II which is described fully by Hansen *et al.* [1983]. GISS II' is a grid point model having 72 and 46 longitudes and latitudes, respectively ($\sim 4^\circ \times 5^\circ$ horizontal resolution), and nine sigma coordinate levels in the vertical with a dynamical top at 10 mbar. The vertical resolution is admittedly crude which has repercussions both for modeling ozone and the prognostic cloud calculations. This point is discussed further in section 4 (conclusions). For the PD run, fixed climatological monthly mean sea surface temperature (SST) data based on the Atmospheric Modeling Intercomparison Project (AMIP) 1979–1993 and ocean ice coverage are incorporated. Tracer advection is achieved via the quadratic upstream method [Prather, 1996] which produces little numerical noise and realistically maintains strong tracer gradients. Further details may be found in the companion paper in part 1 [Shindell *et al.*, 2001] (hereafter referred to as part 1).

We employ 10 chemical tracers (O_x , NO_x , N_2O_5 , HNO_3 , H_2O_2 , CH_3OOH , $HCHO$, HO_2NO_2 , CO , and H_2O) using the “family” approach where appropriate with 37 reactions for 24 molecules [DeMore *et al.*, 1997]. Peroxyacetyl nitrate (PAN) and explicit NMHC chemistry is omitted. A proxy for CO (60 Tg C yr^{-1} , i.e., 10% of the isoprene burden) based on Wang *et al.* [1998] is included. Other NMHC chemistry is omitted. We therefore tend to underestimate ozone production, especially in the PBL. Our “end product” proxy approach for isoprene ignores ozone production via the intermediate oxidation channel $RO_2 + NO$. Other than isoprene, “equivalent CO” for other NMHCs was not included. The FASTJ photolysis scheme, after validation with results from the Photochemical Model Intercomparison (PhotoComp [Olson *et al.*, 1997]), is employed. The chemical and dynamical time steps are 1 hour, 5 min, respectively. N_2O_5 hydrolysis on sulfate aerosol is calculated according to Dentener and Crutzen [1993] using monthly mean modeled sulfate surface area taken from Koch *et al.* [1999]. Wet and dry deposition are adapted from Wang *et al.* [1998]. The lightning parametrization generates NO_x interactively with the convection scheme [Price *et al.*, 1997]. Other chemical emissions are prescribed as monthly mean values and include CO (biomass, equivalent isoprene, and industrial) and NO_x (industrial) adapted from Wang *et al.* [1998]; NO_x aircraft fleet emissions for 1992 [Baughcum *et al.*, 1996; Schulte *et al.*, 1997], and NO_x soil emissions adapted from the GEIA $1^\circ \times 1^\circ$ database. Emission inventories are climatological where possible. Further details may be found in part 1. As described there, the model does a good job of reproducing PD observations of O_x , and based on the lifetime of methyl chloroform, yields a good global OH field.

All runs begin December 1 and were 10 years in duration. Initial analyses suggested a spin-up time of 1 year and 2 years for the control run and for all remaining runs, respectively. Data obtained during spin-up were subsequently discarded. All figures show January and July zonal mean values unless otherwise indicated. Table 1 gives an overview of the runs. Run 1 is the PD control run. Run 2 is our best estimate of PI conditions. It featured chemical emissions, GHGs (CO_2 , CH_4 , and N_2O), and sulfate aerosol reduced from PD to PI conditions. Industrial and aircraft CO and NO_x emissions were set to zero; methane in the chemistry scheme was reduced from 1.803 ppbv (SH equal to 1.750, NH equal to 1.855) to 0.730 ppbv in both hemispheres; biomass burning emissions were set to 10% of their PD value but retaining the same geographical distribution [Wang and Jacob, 1998], and sulfate aerosol was changed to a PI distribution based on the GCM sulfur-cycle model described by Koch *et al.* [1999]. These implied very large, widespread increases (up to 5000%) in sulfate since the PI era over industrialized areas, especially in NH summer. Run 2 also featured specified climatological monthly mean SSTs and ocean ice data, but these were modified from PD to PI (1850) conditions. The 1850 ocean data were obtained from a previous integration of the GCM at $8 \times 10^\circ$ horizontal resolution which calculated rates of ocean heat fluxes (the “qflux” scheme) for the PI atmosphere [Hansen *et al.*, 1983; Russell *et al.*, 1985]. Part 1 gives further information.

Runs 3–5 are sensitivity runs (see Table 1). Run 3 most closely resembles other works in the literature investigating ozone change since the PI era in that it features PI chemical emissions but has PD sulfate aerosol and ocean data. Run 4 tests the effect of reducing sulfate aerosol in run 3 to PI conditions. Run 5 tests the effect of changing the ocean data in run 4 from PD to PI conditions. When calculating O_x burdens in the troposphere, we defined the tropopause using a cutoff criteria of 150 ppb ozone. Changing this value by $\pm 10\%$ led to changes in the burden of $+3/-4\%$, respectively.

3. Results and Discussion

Table 2 shows a complete overview of the global tracer chemical budget. The values in parentheses represent (PD – PI)/PI expressed as a percentage. O_x (obtained separately as the tropospheric burden) and global OH concentrations are discussed separately in the sections which follow. First, a general feature in Table 2 is enhanced wet deposition for the warmer, damper PD atmosphere. Second, all tracers show increases in the PD run occurring mainly in the NH. The increases in NO_x , HNO_3 , HO_2NO_2 , and CO are almost entirely associated with changes in precursor emissions (run 3). Increases in H_2O_2 , CH_3OOH , and $HCHO$ since PI are also chiefly associated with precursor emission changes but also have an added component ($\sim 5\text{--}15\%$) associated with warming the ocean/moistening the atmosphere (run 5).

Table 2. Overview of Global, Annual Mean Chemical Tracer Budget

	Units	Process/Concentration	Global	NH	SH
Run 1 (PD control)					
O _x	10 ³ kg s ⁻¹	dry deposition	-36.1	-23.7	-12.5
O _x	10 ⁴ kg s ⁻¹	chemistry	1.2	1.3	-0.07
NO _x	10 ⁻¹¹ ppv	mixing ratio	35.8	40.9	30.8
NO _x	10 ⁰ kg s ⁻¹	dry deposition	-168.0	-146.1	-21.9
NO _x	10 ⁰ kg s ⁻¹	chemistry	-1,046.7	-842.2	-204.6
NO _x	10 ⁰ kg s ⁻¹	lightning	122.5	73.6	48.9
NO _x	10 ⁰ kg s ⁻¹	surface	1,072.7	898.5	174.2
HNO ₃	10 ⁻¹¹ ppv	mixing ratio	155.6	182.2	128.9
HNO ₃	10 ⁰ kg s ⁻¹	moist convection	-928.2	-564.6	-363.6
HNO ₃	10 ⁰ kg s ⁻¹	wet deposition	-898.3	-774.6	-123.7
HNO ₃	10 ⁰ kg s ⁻¹	dry deposition	-1,949.9	-1,655.5	-294.4
HNO ₃	10 ⁰ kg s ⁻¹	chemistry	4,678.4	3,757.3	921.1
H ₂ O ₂	10 ⁻¹¹ ppv	mixing ratio	106.7	119.3	94.2
H ₂ O ₂	10 ⁰ kg s ⁻¹	moist convection	-5,557.2	-2,939.0	-2,618.2
H ₂ O ₂	10 ⁰ kg s ⁻¹	wet deposition	-1,064.7	-579.8	-484.9
H ₂ O ₂	10 ⁰ kg s ⁻¹	dry deposition	-278.1	-156.0	-122.0
H ₂ O ₂	10 ⁰ kg s ⁻¹	chemistry	11,379.0	6,045.0	5,334.0
N ₂ O ₅	10 ⁻¹ kg s ⁻¹	chemistry	93.0	95.0	-2.0
CH ₃ OOH	10 ⁻¹¹ ppv	mixing ratio	24.9	24.7	25.1
CH ₃ OOH	10 ⁰ kg s ⁻¹	dry deposition	-737.2	-363.1	-374.1
CH ₃ OOH	10 ⁰ kg s ⁻¹	chemistry	757.8	337.8	420.0
HCHO	10 ⁻¹² ppv	mixing ratio	141.0	177.6	104.3
HCHO	10 ⁻¹ kg s ⁻¹	moist convection	41.7	70.1	-28.3
HCHO	10 ⁻¹ kg s ⁻¹	wet deposition	-446.8	-316.4	-130.4
HCHO	10 ⁻¹ kg s ⁻¹	dry deposition	-4,106.2	-2,792.2	-1,314.0
HCHO	10 ⁻¹ kg s ⁻¹	chemistry	5,434.0	3,555.0	1,880.0
HO ₂ NO ₂	10 ⁻¹² ppv	mixing ratio	28.4	35.5	21.3
HO ₂ NO ₂	10 ⁰ kg s ⁻¹	chemistry	-2.2	3.9	-6.2
CO	10 ⁻⁸ ppv	mixing ratio	8.3	10.2	6.4
CO	10 ² kg s ⁻¹	chemistry	-355.2	-249.4	-105.8
H ₂ O	10 ⁻⁴ ppv	mixing ratio	7,839.0	4,272.8	3,566.2
Run 2 (best PI)					
O _x	10 ³ kg s ⁻¹	dry deposition	-20.0 (81%)	-11.2 (112%)	-8.9 (41%)
O _x	10 ⁴ kg s ⁻¹	chemistry	-0.5 (-361%)	-0.09 (1572%)	-0.4 (-82%)
NO _x	10 ⁻¹¹ ppv	mixing ratio	32.1 (12%)	33.9 (21%)	30.4 (1%)
NO _x	10 ⁰ kg s ⁻¹	dry deposition	-31.5 (433%)	-21.2 (589%)	-10.2 (115%)
NO _x	10 ⁻¹ kg s ⁻¹	chemistry	-2,892.6 (262%)	-1,804.4 (367%)	-1,088.2 (88%)
NO _x	10 ⁻¹ kg s ⁻¹	lightning	1,130.2 (8%)	657.1 (12%)	473.1 (3%)
NO _x	10 ⁻¹ kg s ⁻¹	surface	2,115.8 (407%)	1,384.5 (549%)	731.2 (138%)
HNO ₃	10 ⁻¹¹ ppv	mixing ratio	129.3 (20%)	136.3 (34%)	122.2 (5%)
HNO ₃	10 ⁰ kg s ⁻¹	moist convection	-491.3 (89%)	-243.0 (132%)	-248.3 (46%)
HNO ₃	10 ⁰ kg s ⁻¹	wet deposition	-189.5 (374%)	-123.1 (529%)	-66.4 (86%)
HNO ₃	10 ⁰ kg s ⁻¹	dry deposition	-475.4 (310%)	-330.1 (402%)	-145.4 (102%)
HNO ₃	10 ⁰ kg s ⁻¹	chemistry	1,299.7 (260%)	810.2 (364%)	489.5 (88%)
H ₂ O ₂	10 ⁻¹¹ ppv	mixing ratio	56.7 (88%)	59.5 (101%)	53.9 (75%)
H ₂ O ₂	10 ⁰ kg s ⁻¹	moist convection	-3,556.9 (56%)	-1,667.6 (76%)	-1,889.3 (39%)
H ₂ O ₂	10 ⁰ kg s ⁻¹	wet deposition	-563.8 (89%)	-248.9 (133%)	-314.9 (54%)
H ₂ O ₂	10 ⁰ kg s ⁻¹	dry deposition	-1,672.4 (-83%)	-904.8 (-83%)	-767.6 (-84%)
H ₂ O ₂	10 ⁰ kg s ⁻¹	chemistry	6971.0 (63%)	3449.0 (75%)	3522.0 (51%)
N ₂ O ₅	10 ⁻¹ kg s ⁻¹	chemistry	-6.3 (-1576%)	-2.1 (-4624%)	-4.2 (110%)
CH ₃ OOH	10 ⁻¹¹ ppv	mixing ratio	10.0 (149%)	9.7 (155%)	10.2 (146%)
CH ₃ OOH	10 ⁰ kg s ⁻¹	dry deposition	-328.3 (125%)	-163.4 (122%)	-164.9 (127%)
CH ₃ OOH	10 ⁰ kg s ⁻¹	chemistry	332.5 (128%)	166.1 (103%)	166.5 (152%)
HCHO	10 ⁻¹² ppv	mixing ratio	51.6 (173%)	58.8 (202%)	44.5 (134%)
HCHO	10 ⁻¹ kg s ⁻¹	moist convection	-13.3 (-414%)	11.7 (499%)	-25.1 (13%)
HCHO	10 ⁻¹ kg s ⁻¹	wet deposition	-117.4 (281%)	-68.2 (364%)	-49.2 (165%)
HCHO	10 ⁻¹ kg s ⁻¹	dry deposition	-1,293.0 (218%)	-784.5 (256%)	-508.4 (158%)
HCHO	10 ⁻¹ kg s ⁻¹	chemistry	1,720.0 (216%)	1,010.0 (252%)	710.0 (165%)
HO ₂ NO ₂	10 ⁻¹² ppv	mixing ratio	16.3 (74%)	16.9 (110%)	15.7 (36%)
HO ₂ NO ₂	10 ⁰ kg s ⁻¹	chemistry	-4.6 (-52%)	-2.4 (-263%)	-2.2 (182%)
CO	10 ⁻⁸ ppv	mixing ratio	2.7 (207%)	2.8 (264%)	2.7 (137%)
CO	10 ² kg s ⁻¹	chemistry	-72.9 (387%)	-37.4 (567%)	-35.5 (198%)
H ₂ O	10 ⁻⁴ ppv	mixing ratio	6,859.1 (14%)	3,718.3 (15%)	3,140.8 (14%)
Run 3 (PI emissions)					
O _x	10 ³ kg s ⁻¹	dry deposition	-19.7 (83%)	-11.2 (116%)	-8.7 (43%)
O _x	10 ³ kg s ⁻¹	chemistry	-6.4 (-291%)	-1.6 (-925%)	-4.9 (-86%)
NO _x	10 ⁻¹¹ ppv	mixing ratio	32.0 (12%)	33.8 (21%)	30.3 (2%)
NO _x	10 ⁰ kg s ⁻¹	dry deposition	-31.8 (428%)	-21.4 (583%)	-10.4 (111%)
NO _x	10 ⁰ kg s ⁻¹	chemistry	-299.4 (250%)	-187.8 (347%)	-111.6 (83%)
NO _x	10 ⁰ kg s ⁻¹	lightning	121.9 (0.5%)	73.3 (0.5%)	48.7 (0.5%)
HNO ₃	10 ⁻¹¹ ppv	mixing ratio	130.1 (20%)	137.0 (33%)	123.3 (5%)
HNO ₃	10 ⁰ kg s ⁻¹	moist convection	-498.1 (86%)	-256.6 (120%)	-241.5 (50%)

Table 2. (continued)

	Units	Process/Concentration	Global	NH	SH
Run 3 (PI emissions)					
HNO ₃	10 ⁰ kg s ⁻¹	dry deposition	-496.4 (293%)	-339.6 (387%)	-156.7 (88%)
HNO ₃	10 ⁰ kg s ⁻¹	chemistry	1,345.6 (248%)	842.3 (346%)	503.4 (83%)
H ₂ O ₂	10 ⁻¹¹ ppv	mixing ratio	65.8 (62%)	68.7 (74%)	63.0 (50%)
H ₂ O ₂	10 ⁰ kg s ⁻¹	moist convection	-3,876.5 (43%)	-1,931.0 (52%)	-1,945.6 (35%)
H ₂ O ₂	10 ⁰ kg s ⁻¹	wet deposition	-695.4 (53%)	-348.9 (66%)	-346.5 (40%)
H ₂ O ₂	10 ⁰ kg s ⁻¹	dry deposition	-1,855.2 (-85%)	-967.4 (-84%)	-887.7 (-86%)
H ₂ O ₂	10 ⁰ kg s ⁻¹	chemistry	7748.0 (47%)	3831.0 (58%)	3917.0 (36%)
N ₂ O ₅	10 ⁻¹ kg s ⁻¹	chemistry	-8.0 (-1263%)	-3.5 (-2814)	-4.6 (-57%)
CH ₃ OOH	10 ⁻¹¹ ppv	mixing ratio	10.9 (128%)	10.7 (131%)	11.2 (124%)
CH ₃ OOH	10 ⁰ kg s ⁻¹	dry deposition	-348.6 (111%)	-170.1 (113%)	-178.5 (110%)
CH ₃ OOH	10 ⁰ kg s ⁻¹	chemistry	353.9 (114%)	154.9 (118%)	199.0 (111%)
HCHO	10 ⁻¹² ppv	mixing ratio	55.0 (156%)	62.3 (185%)	47.7 (119%)
HCHO	10 ⁻¹ kg s ⁻¹	moist convection	-2.6 (-1704%)	11.3 (520%)	-13.9 (104%)
HCHO	10 ⁻¹ kg s ⁻¹	wet deposition	-134.6 (232%)	-80.8 (292%)	-53.8 (142%)
HCHO	10 ⁻¹ kg s ⁻¹	dry deposition	-1,342.6 (206%)	-812.7 (244%)	-529.8 (148%)
HCHO	10 ⁻¹ kg s ⁻¹	chemistry	1805.0 (201%)	1033.0 (244%)	772.0 (144%)
HO ₂ NO ₂	10 ⁻¹² ppv	mixing ratio	16.2 (75%)	16.8 (111%)	15.6 (37%)
HO ₂ NO ₂	10 ⁰ kg s ⁻¹	chemistry	-5.2 (-58%)	-1.2 (-425%)	-4.1 (51%)
CO	10 ⁻⁸ ppv	mixing ratio	2.8 (196%)	2.8 (264%)	2.7 (137%)
CO	10 ² kg s ⁻¹	chemistry	-75.2 (372%)	-38.7 (544%)	-36.6 (189%)
H ₂ O	10 ⁻⁴ ppv	mixing ratio	7,804.2 (0.4%)	4,245.7 (0.6%)	3,558.5 (0.2%)
Run 4 (test sulfate)					
O _x	10 ³ kg s ⁻¹	dry deposition	-19.7 (83%)	-11.0 (116%)	-8.8 (42%)
O _x	10 ³ kg s ⁻¹	chemistry	-6.4 (-292%)	-1.5 (-938%)	-4.8 (-86%)
NO _x	10 ⁻¹¹ ppv	mixing ratio	32.0 (12%)	33.8 (21%)	30.3 (2%)
NO _x	10 ⁰ kg s ⁻¹	dry deposition	-31.9 (427%)	-21.4 (583%)	-10.5 (109%)
NO _x	10 ⁰ kg s ⁻¹	chemistry	-299.4 (250%)	-187.6 (349%)	-111.8 (83%)
NO _x	10 ⁰ kg s ⁻¹	lightning	122.1 (0.4%)	73.3 (0.4%)	48.7 (0.3%)
HNO ₃	10 ⁻¹¹ ppv	mixing ratio	130.1 (20%)	136.9 (33%)	123.2 (5%)
HNO ₃	10 ⁰ kg s ⁻¹	moist convection	-496.4 (87%)	-254.9 (121%)	-241.5 (51%)
HNO ₃	10 ⁰ kg s ⁻¹	wet deposition	-213.1 (322%)	-141.5 (447%)	-71.6 (73%)
HNO ₃	10 ⁰ kg s ⁻¹	dry deposition	-496.9 (292%)	-340.0 (387%)	-156.9 (88%)
HNO ₃	10 ⁰ kg s ⁻¹	chemistry	1,346.0 (248%)	841.6 (346%)	504.4 (83%)
H ₂ O ₂	10 ⁻¹¹ ppv	mixing ratio	65.7 (63%)	68.6 (74%)	62.8 (50%)
H ₂ O ₂	10 ⁰ kg s ⁻¹	moist convection	-3,856.8 (44%)	-1,924.5 (53%)	-1,932.3 (35%)
H ₂ O ₂	10 ⁰ kg s ⁻¹	wet deposition	-689.8 (54%)	-343.2 (69%)	-346.1 (40%)
H ₂ O ₂	10 ⁰ kg s ⁻¹	dry deposition	-1,853.2 (-85%)	-967.1 (-84%)	-886.1 (-86%)
H ₂ O ₂	10 ⁰ kg s ⁻¹	chemistry	7,712.0 (48%)	3,814.0 (58%)	3,898.0 (37%)
N ₂ O ₅	10 ⁻¹ kg s ⁻¹	chemistry	-6.6 (-1509%)	-2.3 (-4230%)	-4.3 (-53%)
CH ₃ OOH	10 ⁻¹¹ ppv	mixing ratio	10.9 (128%)	10.7 (131%)	11.2 (124%)
CH ₃ OOH	10 ⁰ kg s ⁻¹	dry deposition	-348.5 (112%)	-170.0 (114%)	-178.5 (110%)
CH ₃ OOH	10 ⁰ kg s ⁻¹	chemistry	353.9 (114%)	154.9 (118%)	199.1 (111%)
HCHO	10 ⁻¹² ppv	mixing ratio	55.1 (156%)	62.4 (185%)	47.7 (119%)
HCHO	10 ⁻¹ kg s ⁻¹	moist convection	-3.4 (-1326%)	11.4 (515%)	-14.9 (90%)
HCHO	10 ⁻¹ kg s ⁻¹	wet deposition	-133.3 (235%)	-80.0 (296%)	-53.2 (145%)
HCHO	10 ⁻¹ kg s ⁻¹	dry deposition	-1,344.8 (205%)	-814.6 (243%)	-530.2 (148%)
HCHO	10 ⁻¹ kg s ⁻¹	chemistry	1,806.0 (201%)	1,037.0 (243%)	769.0 (144%)
HO ₂ NO ₂	10 ⁻¹² ppv	mixing ratio	16.2 (75%)	16.7 (113%)	15.7 (36%)
HO ₂ NO ₂	10 ⁰ kg s ⁻¹	chemistry	-5.7 (-61%)	-1.6 (-344%)	-4.1 (51%)
CO	10 ⁻⁸ ppv	mixing ratio	2.7 (207%)	2.8 (264%)	2.7 (137%)
CO	10 ² kg s ⁻¹	chemistry	-74.1 (379%)	-37.5 (565%)	-36.6 (189%)
H ₂ O	10 ⁻⁴ ppv	mixing ratio	7,790.4 (0.6%)	4,235.3 (0.9%)	3,555.1 (0.3%)
Run 5 (test ocean)					
O _x	10 ³ kg s ⁻¹	dry deposition	-20.0 (80%)	-11.1 (114%)	-8.9 (40%)
O _x	10 ³ kg s ⁻¹	chemistry	-5.2 (-338%)	-1.0 (-1379%)	-4.1 (-84%)
NO _x	10 ⁻¹¹ ppv	mixing ratio	32.1 (12%)	33.8 (21%)	30.4 (1%)
NO _x	10 ⁰ kg s ⁻¹	dry deposition	-31.6 (432%)	-21.2 (589%)	-10.3 (113%)
NO _x	10 ⁰ kg s ⁻¹	chemistry	-290.9 (260%)	-181.4 (364%)	-109.6 (87%)
NO _x	10 ⁰ kg s ⁻¹	lightning	114.7 (7%)	67.2 (10%)	47.6 (3%)
HNO ₃	10 ⁻¹¹ ppv	mixing ratio	129.6 (20%)	136.5 (33%)	122.6 (5%)
HNO ₃	10 ⁰ kg s ⁻¹	moist convection	-492.2 (89%)	-242.2 (133%)	-250.0 (45%)
HNO ₃	10 ⁰ kg s ⁻¹	wet deposition	-192.2 (367%)	-124.1 (524%)	-68.2 (81%)
HNO ₃	10 ⁰ kg s ⁻¹	dry deposition	-479.2 (307%)	-331.4 (400%)	-147.8 (99%)
HNO ₃	10 ⁰ kg s ⁻¹	chemistry	1,307.4 (258%)	814.4 (361%)	493.0 (87%)
H ₂ O ₂	10 ⁻¹¹ ppv	mixing ratio	57.7 (85%)	60.6 (97%)	54.9 (72%)
H ₂ O ₂	10 ⁰ kg s ⁻¹	moist convection	-3,526.8 (58%)	-1,653.5 (58%)	-1,872.3 (40%)
H ₂ O ₂	10 ⁰ kg s ⁻¹	wet deposition	-569.4 (87%)	-250.3 (132%)	-319.2 (52%)
H ₂ O ₂	10 ⁰ kg s ⁻¹	dry deposition	-1,695.9 (-84%)	-914.3 (-83%)	-781.7 (-84%)
H ₂ O ₂	10 ⁰ kg s ⁻¹	chemistry	6,985.0 (63%)	3,451.0 (75%)	3,534.0 (51%)
N ₂ O ₅	10 ⁻¹ kg s ⁻¹	chemistry	-6.4 (-1553%)	-2.2 (-4418%)	-4.2 (-52%)

Table 2. (continued)

	Units	Process/Concentration	Global	NH	SH
Run 5 (test ocean)					
CH ₃ OOH	10 ⁻¹¹ ppv	mixing ratio	10.1 (147%)	9.9 (150%)	10.3 (144%)
CH ₃ OOH	10 ⁰ kg s ⁻¹	dry deposition	-330.7 (123%)	-164.5 (121%)	-166.2 (125%)
CH ₃ OOH	10 ⁰ kg s ⁻¹	chemistry	335.5 (126%)	164.7 (105%)	170.7 (146%)
HCHO	10 ⁻¹² ppv	mixing ratio	52.9 (167%)	59.4 (199%)	45.0 (132%)
HCHO	10 ⁻¹ kg s ⁻¹	moist convection	-7.9 (-628%)	14.7 (377%)	-22.9 (24%)
HCHO	10 ⁻¹ kg s ⁻¹	wet deposition	-118.0 (279%)	-68.4 (363%)	-49.7 (162%)
HCHO	10 ⁻¹ kg s ⁻¹	dry deposition	-1,301.4 (216%)	-789.7 (254%)	-511.7 (157%)
HCHO	10 ⁻¹ kg s ⁻¹	chemistry	1,728.0 (214%)	1,009.0 (252%)	719.0 (161%)
HO ₂ NO ₂	10 ⁻¹² ppv	mixing ratio	16.4 (73%)	16.8 (111%)	15.9 (34%)
HO ₂ NO ₂	10 ⁰ kg s ⁻¹	chemistry	-4.8 (-54%)	-2.3 (-270%)	-2.5 (148%)
CO	10 ⁻⁸ ppv	mixing ratio	2.7 (207%)	2.8 (264%)	2.7 (137%)
CO	10 ² kg s ⁻¹	chemistry	-73.2 (385%)	-37.3 (569%)	-35.9 (195%)
H ₂ O	10 ⁻⁴ ppv	mixing ratio	6,914.6 (13%)	3,758.0 (14%)	3,156.6 (13%)

O_x chemical production is negative in all hemispheres for all PI runs but strongly positive for the PD run in the NH. The cold ocean (run 5), with 13% less water vapor than the PD run, features around 20% more O_x chemical production than other PI runs not having the cold ocean, due to a weaker O¹D + H₂O sink. The lowered sulfate run (run 4) led to a significant slowing in the global mean rate of N₂O₅ chemical destruction, from -0.8 to -0.66 Kg s⁻¹ in runs 3 and 4 but otherwise had little impact. However, more significant effects are apparent when zonal mean difference plots are obtained (section 3.2). Global lightning increased by 8% in going from the best PI (run 2) to the PD, 7% of which was associated with changing the ocean data (run 5). Global water vapor similarly increased by 14%, 13% of which was associated with changing the ocean data. Changes due to chemistry became generally stronger (i.e., stronger destruction of NO_x and CO, stronger production of the other tracers) in going from PI to PD. The exception was HO₂NO₂ which featured overall weaker chemical destruction for the PD run (e.g., by 52% compared with the best PI, run 2), and displayed increased PD production in the NH associated with increased NO_x yet increased destruction in the SH probably associated with enhanced thermal decomposition in the warmer PD atmosphere. Changing to PI ocean data had only a small effect (a couple of percent at most) upon the chemistry terms in run 1, except for O_x, which increased by around 20% due to the suppressed O¹D + H₂O sink, as already mentioned.

Table 3 assesses model internal variability by presenting confidence intervals at 99, 95, and 60% calculated from the *t* distribution based on eight Julys for NO_x, NO_x from lightning, OH, H₂O, and tropospheric ozone. Data are shown for run 4 although all PI runs displayed similar internal variability. Table 3 data are considered in the sections which follow, in which we mainly discuss changes due to ozone and OH in the zonal mean for the various runs.

An interesting application of coupled chemistry-climate models is to quantify changes in the downward fluxes of O_x and NO_x from the stratosphere to the troposphere. Table 4 presents vertical mass fluxes for these two families between level 7 and level 8 (mean pressure equal to 110 mbar). The same definition was applied in part 1. The values in parentheses represent (PD - PI)/PI expressed as a percentage, as for Table 2. Results in Table 4 suggest that in going from PI to PD, the net downward transport of O_x from the stratosphere has generally slowed (e.g., by 3.6% for the best PI estimate, run 2) whereas that for NO_x has increased (e.g., by 37.5% for run 2). Further, the O_x changes appear to be driven mainly by changes

in the emissions (run 3) and occur more strongly in the NH, whereas the NO_x changes are driven mainly by changing the ocean data (run 5) and occur more strongly in the SH. Since NO_x and O_x are fixed and proportional to each other in the stratosphere, the differing response reflects changes in the upward, rather than the downward fluxes. A slowing in net downward O_x in Table 4, controlled mainly by emissions, is consistent with higher values of O_x, hence an increased upward flux in PD. An increase in net downward NO_x, controlled mainly by the ocean data, is consistent with a damper atmosphere leading to faster loss of NO_x into HNO₃ in PD, hence a slower upward flux. Changing the sulfate aerosol has only a small effect (compare runs 3 and 4).

3.1. Control (Run 1) Versus Best PI (Run 2)

Figure 1 shows O_x (ppbv) for the control (run 1), while Figure 2 shows the difference in O_x (ppbv) for run 1 and run 2 (best PI) (annual averages were shown in part 1). The total tropospheric O_x burden for runs 1 and 2 (Table 5) was 423 and 306 teragrams (Tg) respectively, i.e., an increase of 38% (significant to >99%, Table 3) from PI to PD. Peak differences of 30–40 ppbv occur in the NH during July throughout much of the troposphere.

The winter hemisphere in Figure 2 displays anomalous, negative (5–10 ppbv) (PD - PI) O_x features near the tropopause. Figure 3 shows one standard deviation O_x of eight Julys for the control run on levels one and seven. January values (not shown) were generally lower by around 10% in the NH and were similar in the SH. Standard deviation values on the model sigma levels are enhanced over high terrain, e.g., Greenland and Antarctica where absolute O_x values are high. Also, level seven (202 mbar) values are much higher (20–50 ppbv) than those on level 1 (959 mbar) which are typically 0–15 ppbv. The negative O_x features near the tropopause are only of the order 1σ. However, note that the radiative forcing is most sensitive in regions where these features occur and there does exist a possible physical explanation for their occurrence: NO_x differences (ppt) for (control PD and best PI), i.e. (run 1 and run 2) (not shown), indicated higher PI NO_x near the tropopause but not exactly at those latitudes corresponding to the O_x anomalies. Further investigation discounted stratospheric-tropospheric exchange as being the source of the high NO_x features. The chemistry scheme was the main contributor. The features corresponded reasonably well (but not exactly) to PI HNO₃, which was lowered in these regions by roughly an equal magnitude. This then suggests that lowered PI OH was playing a

Table 3. The 60, 95, and 99% Level Confidence Intervals (*t* Distribution) for Eight Julys (Run 4)

Confidence Level	Confidence Interval				
	NO _x , ppt Mean Equal to 33.2	NO _x From Lightning, kg s ⁻¹ grid box ⁻¹ Mean Equal to 153.2	OH, molecules cm ⁻³ Mean Equal to 14.3	H ₂ O, 1 × 10 ⁻⁴ vmr Mean Equal to 114.3	O _x Tropospheric Burden, Tg Mean Equal to 305
60%	global equal to 33.1 → 33.3 NH equal to 36.5 → 36.7 SH equal to 29.7 → 29.8	global equal to 151.1 → 155.3 NH equal to 126.2 → 130.6 SH equal to 24.4 → 25.0	global equal to 14.2 → 14.2 NH equal to 21.0 → 21.2 SH equal to 7.5 → 7.5	global equal to 114.1 → 114.5 NH equal to 74.5 → 74.9 SH equal to 39.5 → 39.7	global equal to 304.3 → 305.5
95%	global equal to 33.0 → 33.4 NH equal to 36.3 → 36.9 SH equal to 29.6 → 29.9	global equal to 147.6 → 158.7 NH equal to 122.7 → 134.1 SH equal to 23.8 → 25.6	global equal to 14.2 → 14.3 NH equal to 20.9 → 21.3 SH equal to 7.4 → 7.5	global equal to 113.9 → 114.7 NH equal to 74.2 → 75.2 SH equal to 39.3 → 39.9	global equal to 303.6 → 306.6
99%	global equal to 32.9 → 33.5 NH equal to 36.2 → 37.1 SH equal to 29.6 → 29.9	global equal to 145.0 → 161.4 NH equal to 120.0 → 136.9 SH equal to 23.4 → 26.1	global equal to 14.1 → 14.4 NH equal to 20.9 → 21.3 SH equal to 7.4 → 7.6	global equal to 113.6 → 114.9 NH equal to 73.9 → 75.4 SH equal to 39.2 → 40.0	global equal to 302.6 → 307.3

role. The features were not exactly colocated since HNO₃ has a longer lifetime than NO_x and is affected by large-scale dynamics to a greater extent. The sign of (PD – PI) OH change in the real atmosphere is uncertain due to opposing chemical effects, as discussed in the introduction. Lightning in the tropics also played a lesser role (not shown) occasionally leading to higher PI NO_x in some regions but more usually resulting in lowered NO_x. Run 1 (control) and run 2 (best PI estimate) featured 3.87 (NH equal to 2.33, SH equal to 1.55) and 3.57 (NH equal to 2.08, SH equal to 1.49) Tg N yr⁻¹, respectively. Such a lowering of 8% is significant at the 99% confidence interval (Table 3). The bulk of the decrease was due to changing the ocean data from PD to PI conditions, as will be shown in section 3.2.3. Another possible cause of high PI ozone is enhanced clouds leading to a lowered *j*O¹D sink. However, clouds only increased in a narrow latitude belt centred over the equator (Figure 13); since the high PI ozone occurred mainly at mid to high latitudes, clouds were concluded not to play a role.

Figure 4 shows OH (1 × 10⁵ molecules cm⁻³) for run 1, while Figure 5 shows the difference (1 × 10⁵ molecules cm⁻³) for OH (run 1 – run 2), i.e. (PD control – best PI). Annual averages were shown in part 1. Global mean OH values for runs 1 and 2 (Table 3) were 9.8 (NH equal to 12.0, SH equal to 7.6) × 10⁵ molecules cm⁻³ (almost the very same value of 9.7 was derived by *Prinn et al.* [1995] using CH₃CCl₃ measurements between 1978 and 1994) and 10.2 (NH equal to 12.0, SH equal to 8.4) × 10⁵ molecules cm⁻³ respectively, i.e., a decrease of 3.9% (NH equal to 0.0%, SH equal to 9.5%) from PI to PD, which is significant at the 99% confidence interval (Table 3). PI OH is generally higher than PD throughout the tropical troposphere except at (1) higher levels especially in summer and (2) near the ground especially between the tropics and midlatitudes. Higher PI OH is associated with lower CO and occurs despite lower NO_x and lower water vapor; PD water column (mm) is equal to 22.51 (NH equal to 23.11, SH equal to 21.92), whereas PI water column is equal to 19.49 (NH equal to 19.71, SH equal to 19.27).

Figure 6 shows the difference (tenths °C) in temperature for (PD control – best PI), i.e. (run 1 – run 2). Stratospheric cooling leads to a 1°–2°C lowering in temperature; tropical midtroposphere heating results in 3°–5°C warming. Annual mean surface temperatures increased from 11.390°C (NH equal to 12.546, SH equal to 10.234) in run 2 to 13.343°C (NH equal to 14.333, SH equal to 12.354) in run 1, corresponding to 17.1% (NH equal to 14.2%, SH equal to 20.7%). Note that for the control run, annual mean sigma is equal to 0.025 K; this value is somewhat lower than observations which are in the range 0.2–0.4 K [*Intergovernmental Panel on Climate Change (IPCC)*, 1996]. The discrepancy is associated with fixing SSTs in the model.

Global mean air temperature increases were 1.853°C (NH equal to 1.676, SH equal to 2.030). These were associated mainly with changing the ocean data and were stronger in the SH due to a larger area of ocean coverage. This more than outweighed greater O_x changes in the NH.

The difference (%) in moist convective cloud cover (not shown, but very similar to Figure 11) for run 1 (PD control) – run 2 (best PI) revealed that the equatorial midtroposphere is more cloudy by 2–4% in the PD run ($\sigma_{\text{jan}} = 0.50$, $\sigma_{\text{jul}} = 0.53\%$ at 323 mbar). This region is straddled north and south by features for which the opposite is true. We interpret these results as follows: increased PD water vapor in the central

Table 4. Downward Mass Transport for O_x and NO_x Between Layers 7 and 8 (Approximately 110 mbar)^a

Run	O_x Global	O_x NH	O_x SH	NO_x Global	NO_x NH	NO_x SH
1 (PD control)	23,820	11,580	12,180	6.6	2.9	3.8
2 (best PI)	24,720 (−3.6%)	12,360 (−6.3%)	12,360 (−1.4%)	4.8 (37.5%)	2.3 (20.7%)	2.5 (34.2%)
3 (PI emissions)	26,040 (−8.5%)	13,080 (−11.5%)	12,960 (−6.0%)	5.6 (17.9%)	2.8 (3.4%)	2.8 (26.3%)
4 (test sulfate)	26,040 (−8.5%)	13,020 (−11.1%)	12,960 (−6.0%)	5.6 (17.9%)	2.6 (10.3%)	2.9 (23.7%)
5 (test ocean)	25,200 (−5.7%)	12,540 (−7.7%)	12,600 (−3.0%)	4.9 (34.7%)	2.3 (20.7%)	2.6 (31.6%)

^aUnits are in $kg\ s^{-1}$.

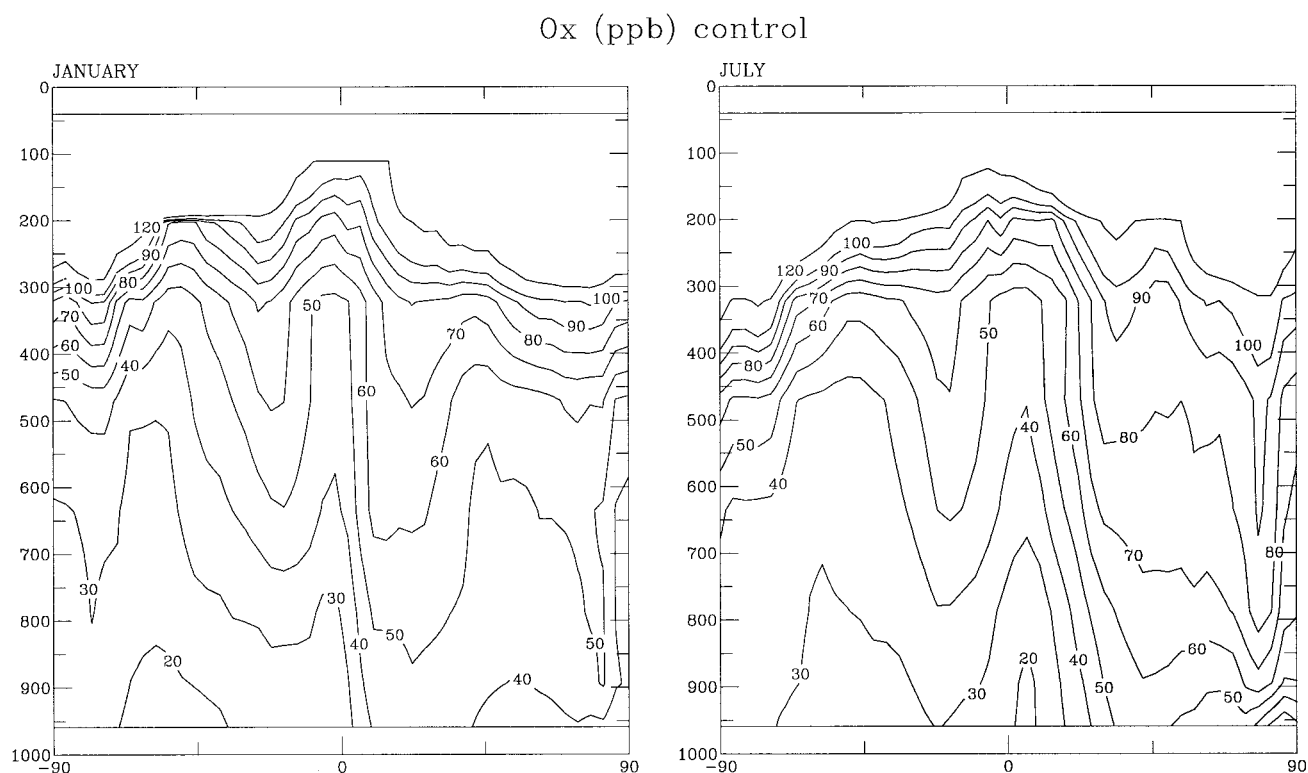
tropics implies extraradiative heating hence decreased stability which strengthens the ascending Hadley cell hence increases moist convective cloud cover. The adjacent, descending arms are also strengthened, which tends to decrease cloud cover in these regions. The changes arise mainly due to changes in the ocean data and also impact upon NO_x from the lightning scheme. They are quantified and discussed further in section 3.2.3, which discusses the effect of the ocean data alone.

3.2. Effect of Precursor Emissions, Sulfate Aerosol, Ocean Data, and GHGs

The only modification to run 3 compared with the PD control (run 1) is a lowering in O_x precursor emissions. Run 3 is therefore the most comparable with other works which simulate O_x increases since the PI era, as discussed in 3.2.1. In 3.2.2 we investigate the effect in run 3 of modifying to PI conditions the sulfate aerosol in the chemistry scheme (run 4); in 3.2.3 we then investigate the effect in run 4 of modifying to PI conditions the ocean data (run 5). The best estimate PI run (run 2) is then obtained by modifying to PI conditions the GHGs in run 5. In 3.2.4 we compare run 2 (best PI) with run 5 which differ only in that run 2 has PI levels of GHGs.

3.2.1. Precursor emissions. Figure 7 shows the difference (ppbv) for O_x run 1 (PD control) – run 3 (PI emissions, i.e., most comparable to other works). Total O_x burdens (Tg) for run 3 (Table 5) were 305 Tg, an increase of 39% from PI to PD. Our percent change value compares reasonably well with other works, e.g. (360.0 to 230.4 Tg), i.e., 56.3% [Mickley *et al.*, 1999] (273.6 to 192.0 Tg), i.e., 42.5% [Roelofs *et al.*, 1997], and (312.0 to 192.0 Tg), i.e., 62.5% [Wang and Jacob, 1998] (see also discussion in part 1). In Table 5 the ozone change for run 3 (PI emissions) is similar to that of run 2 (best PI), and so the precursor emissions are responsible for the bulk of the ozone change. Figure 7 featured an anomalously high PI O_x feature occurring in SH high latitudes (but less prevalent than for the best PI run, Figure 2). This arose due to higher PI NO_x (as for run 2, section 3.1) and was associated with lower PI OH (not shown); again, its magnitude was close to one standard deviation in O_x (Figure 3).

Plotting the difference (1×10^5 molecules cm^{-3}) for OH run 1 (PD control) – run 3 (PI emissions) revealed results (not shown) similar to Figure 5, which showed run 1 (PD control) – run 2 (best PI estimate). The global mean OH value for run 3

**Figure 1.** O_x ($=O_3 + O^1D + O^3P$), ppbv for the control run. Note that the top model level is at 10 mbar.

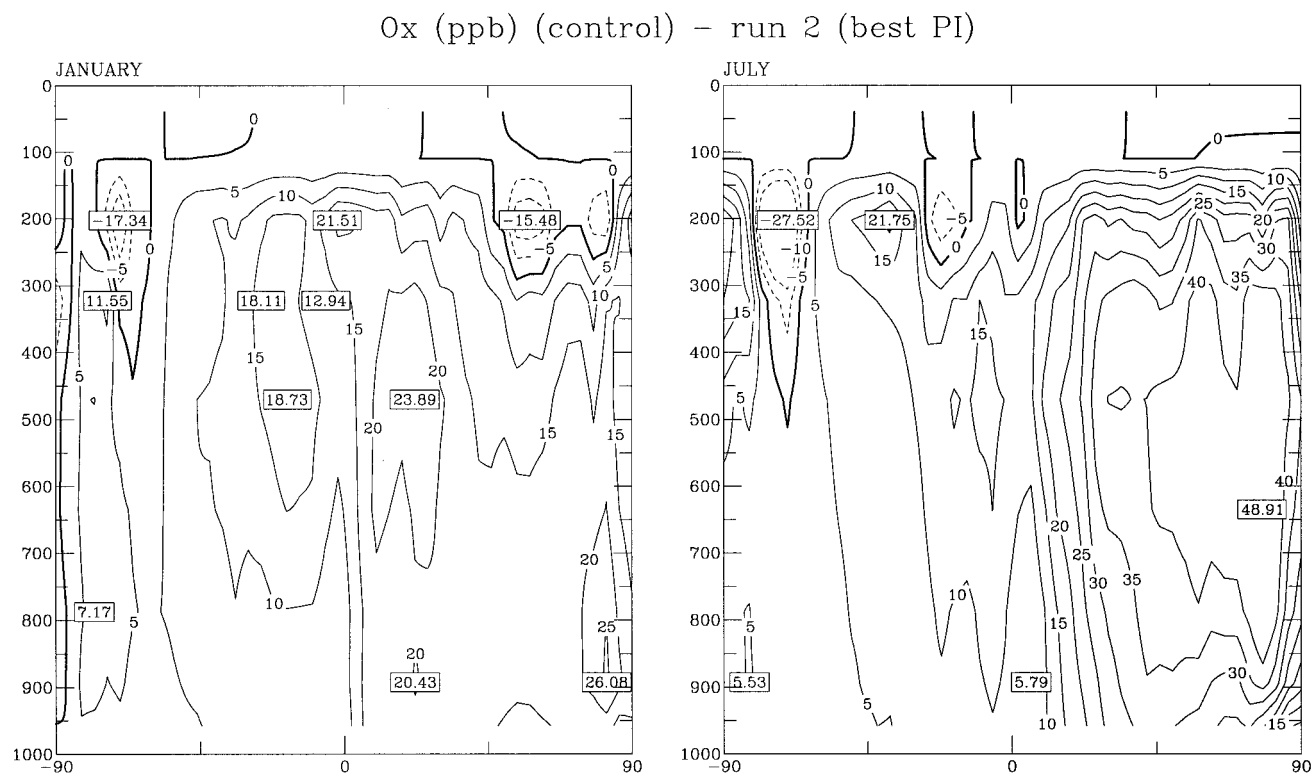


Figure 2. O_x, ppbv for the control – best PI run (run 2).

(Table 5) was 10.6×10^5 molecules cm^{-3} (NH equal to 12.5, SH equal to 8.8) corresponding to a 7.5% (NH equal to 4.0, SH equal to 13.6) decrease from PI to PD, which is significant at the 99% confidence interval (Table 3). Values from other works vary between a 20% increase to a 6–7% decrease [see, e.g., Wang and Jacob, 1998] (or part 1). Wang and Jacob [1998] calculate similar OH changes yet do not calculate the anomalous high PI NO_x and O_x features occurring in SH high latitudes (as discussed in 3.1). Hauglustaine *et al.* [1994] calculate widely different OH spatial changes and also do not calculate the higher PI O_x. Other works report only O_x, not OH [Roelofs *et al.*, 1997; Stevenson *et al.*, 1998; Brasseur *et al.*, 1998; Bernsten *et al.*, 1997], and they too do not report higher PI O_x in SH high

latitudes. Mickley *et al.* [1999] do calculate higher PI NO_x in this region (L. Mickley, personal communication, 2001). However, they do not see higher PI O_x values and have suggested that the NO_x phenomenon is related to PAN formation (not present in our model) being suppressed in remote regions. Grewe *et al.* [2001a] compared GISS modeled NO_x near the tropopause with observed data and found that modeled NO_x reasonably reproduced observations for zonal mean values, but the modeled values failed to capture observed longitudinal variability, possibly reflecting inadequacies in modeled nitrogen oxide chemistry and/or dynamical effects.

3.2.2. Effect of sulfate aerosol. Plotting the difference (ppbv) in O_x for run 4 (PI emissions and PI sulfate) – run 3 (PI

Table 5. Modeled OH and O_x (=O³P + O¹D + O₃)^a

Run	OH, 1×10^5 molecules cm^{-3}	O _x , Tg
Run 1 (PD control run)	9.8 NH equal to 12.0 SH equal to 7.6	423
Run 2 (best estimate of PI)	10.2 (3.9%) NH equal to 12.0 (0.0%) SH equal to 8.4 (9.5%)	306 (38%)
Run 3 (most comparable to other works)	10.6 (7.5%) NH equal to 12.5 (4.0%) SH equal to 8.8 (13.6%)	305 (39%)
Run 4 (test sulfate)	10.7 (8.4%) NH equal to 12.5 (4.0%) SH equal to 8.8 (13.6%)	305 (39%)
Run 5 (test ocean)	10.3 (4.9%) NH equal to 12.2 (1.6%) SH equal to 8.5 (10.6%)	310 (36%)

^aPercent indicates change relative to control.

One standard deviation (ppb) ozone July

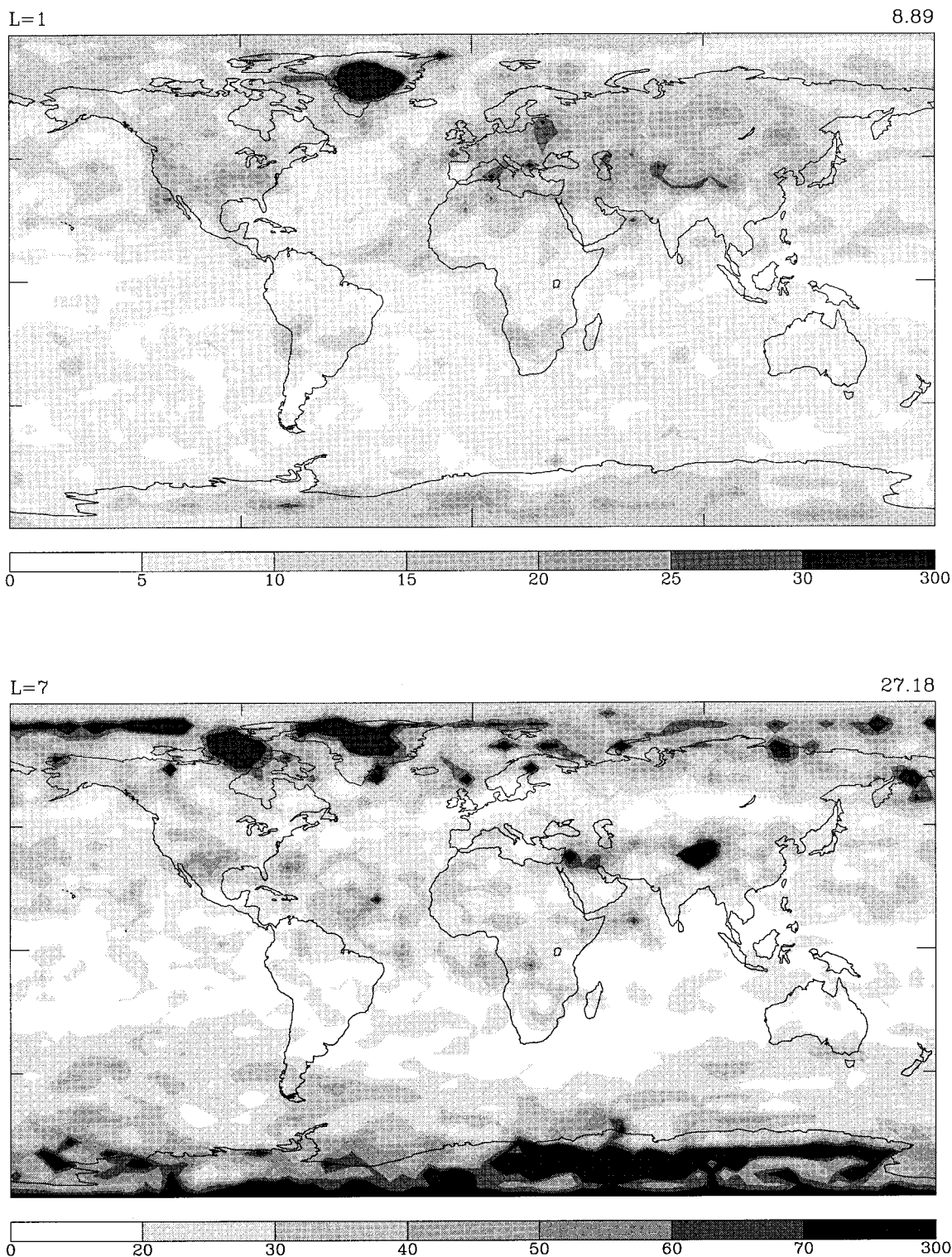


Figure 3. One standard deviation O_x (ppbv) in July, levels 1 and 7.

emissions only) (not shown) revealed mostly small values <2 ppb with higher (up to 10 ppb) values occurring near the tropopause, although these were not statistically significant due to higher concentrations of ozone in this region, as discussed previously. Negative O_x features occurred in the SH in

both winter and summer. Overall, ozone was lowered by 2–3% in the upper troposphere. Figure 8 shows the difference (ppt) for NO_x run 4 (PI emissions and PI sulfate) – run 3 (PI emissions only). Apparent are the succession of positive/negative features near the tropopause. Longer runs are re-

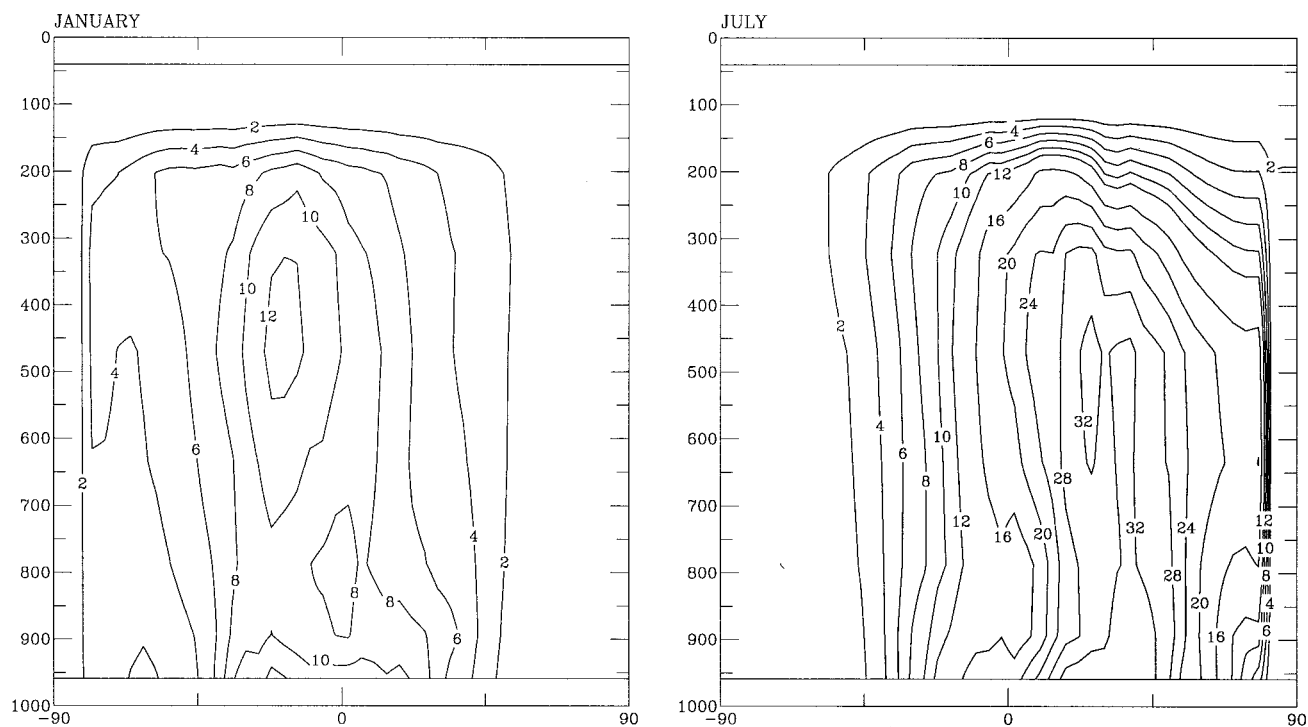
OH ($1.E5$ molec/cc) control

Figure 4. OH (1×10^5 molecules cm^{-3}) for the control run.

quired to establish whether these features have a physical basis or arise via internal model variability. Total O_x burdens for run 4 (Table 5) were 305 Tg, similar to run 3.

Figure 9 shows the difference (1×10^5 molecules cm^{-3}) for

OH run 4 (PI emissions and PI sulfate) – run 3 (PI emissions only). Although global mean OH values were very similar for both runs (Table 5), values did vary quite considerably latitudinally. The complex behavior in the NH we interpret as sul-

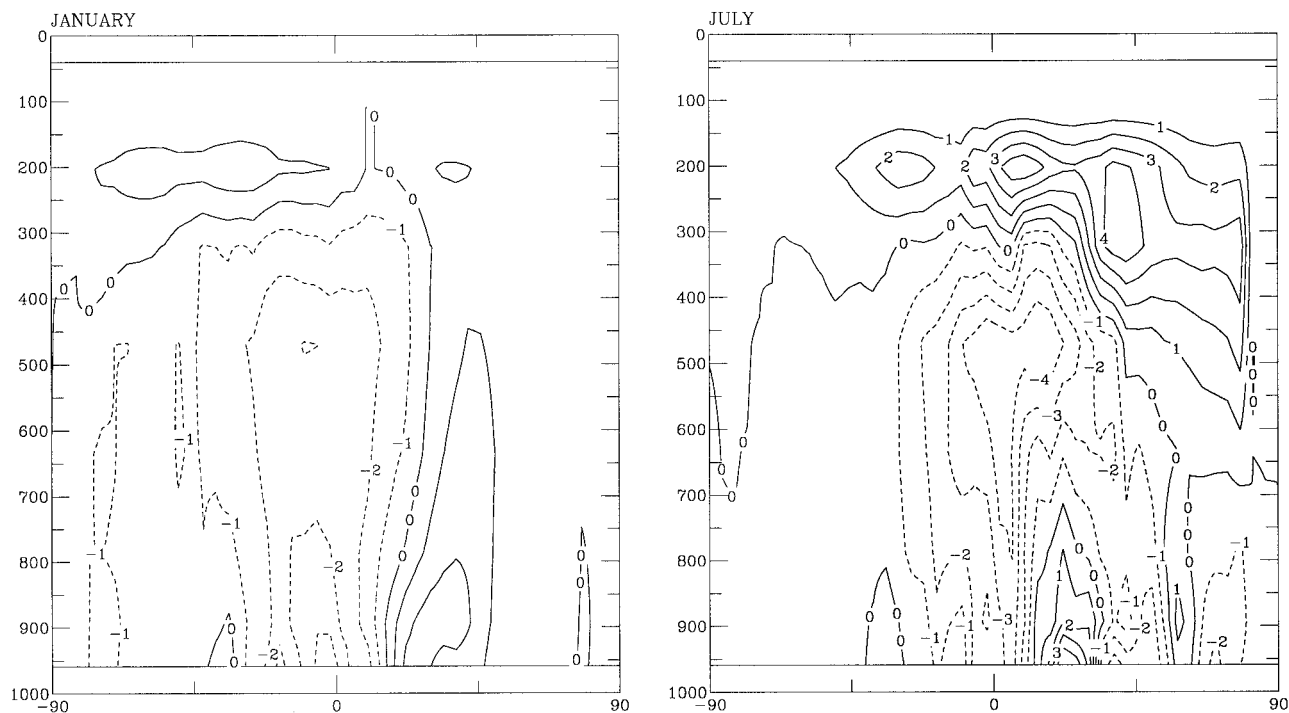
OH ($1.E5$ molec/cc) control – run 2 (best PI)

Figure 5. OH (1×10^5 molecules cm^{-3}) for the control – best PI run (run 2).

Temperature (tenths degree C) control – run 2 (best PI)

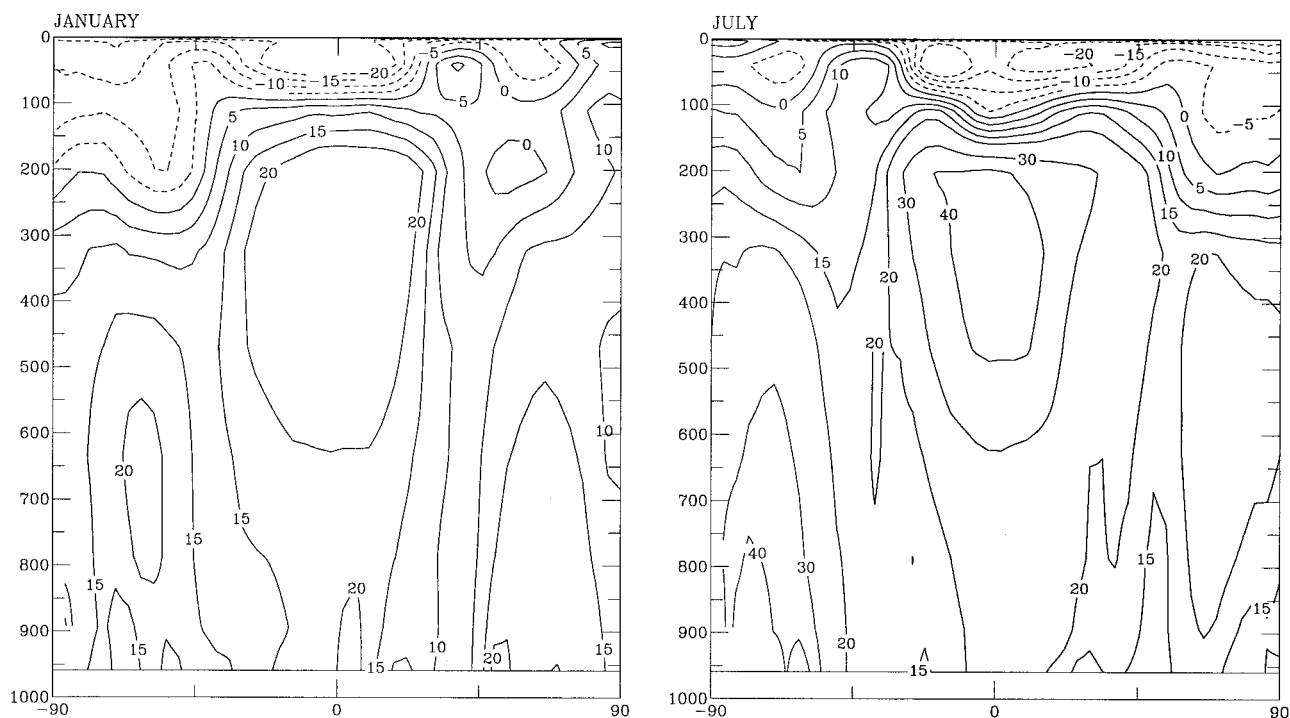


Figure 6. Temperature (tenths °C) for the control – best PI run (run 2).

fate on the one hand lowering OH (lowered NO_x suppresses the reaction $\text{HO}_2 + \text{NO} \rightarrow \text{OH} + \text{NO}_2$) and on the other hand increasing OH (increased HNO_3 photolysis). The vertical band structure is believed to arise due to changes in the Hadley cell

circulation which results in alternately enhanced/depleted regions of cloudiness, which results in decreased/increased UV below cloud height as well as producing modifications in OH concentrations.

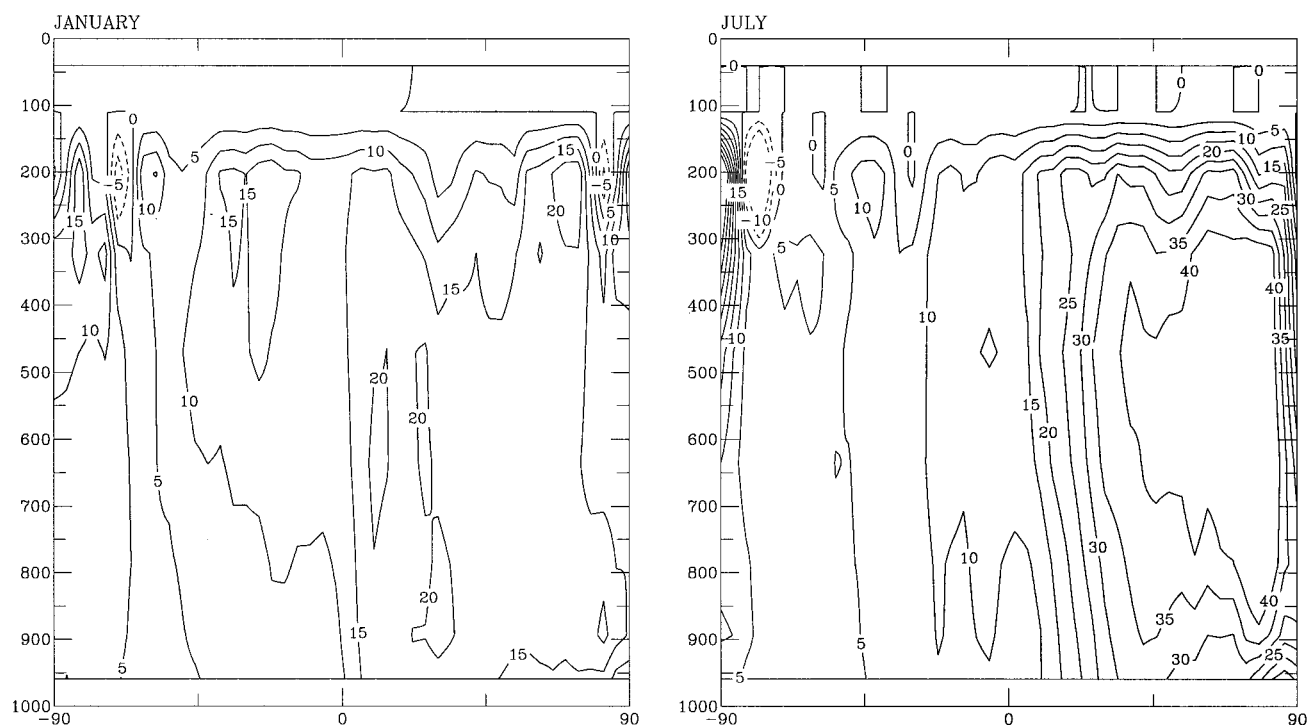
 O_x (ppb) control – run 3 (most comparable to other works)

Figure 7. O_x , ppbv for the control – preindustrial emissions run (i.e., run 3, most comparable to other works).

NO_x (ppt) run 4 (test sulfate) – run 3 (most comparable to other works)

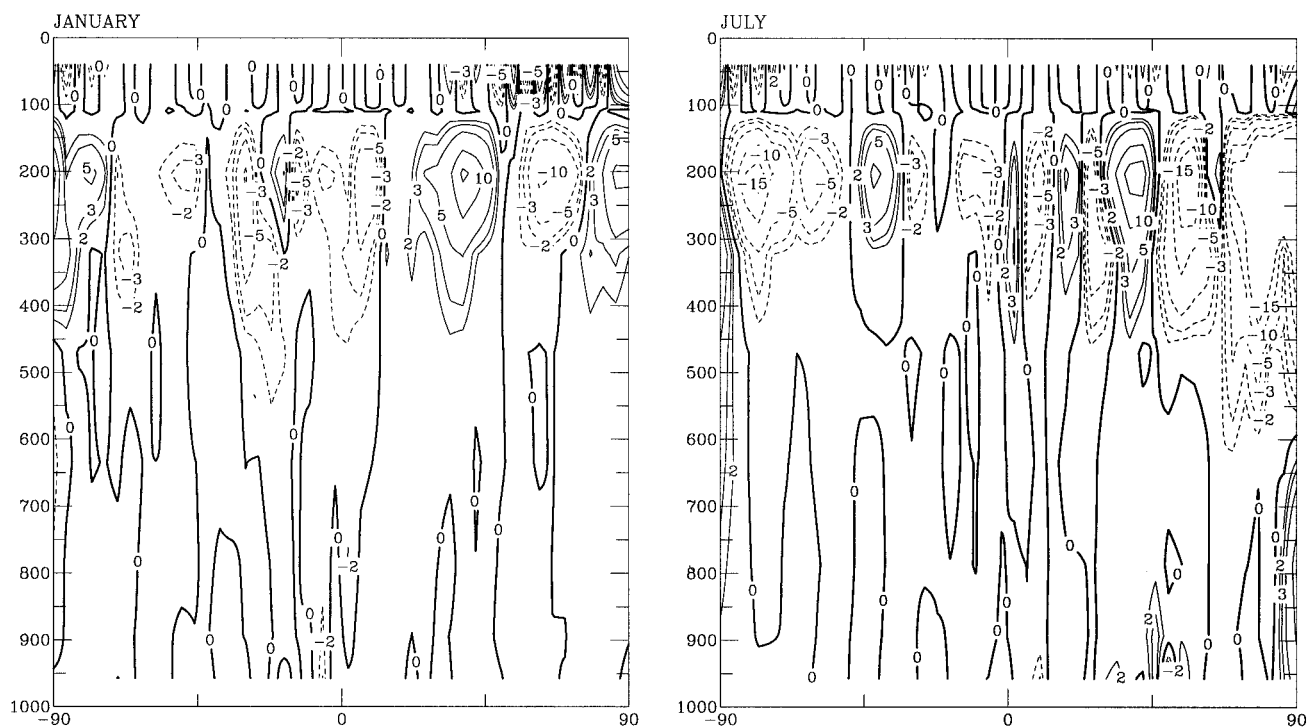


Figure 8. NO_x (ppt) for run 4 (PI sulfate and emissions) – run 3 (PI emissions).

3.2.3. Effect of ocean data. Plotting the difference (ppbv) for O_x run 5 (PI emissions, sulfate, and ocean) – run 4 (PI emissions and sulfate only) revealed a positive feature (up to 20 ppbv) occurring in the tropical upper troposphere during July (not shown). Similar to the features discussed in 3.2.1, its

magnitude is only of the order one standard deviation (Figure 3), so it may have arisen via model variability. However, there is a possible physical explanation, namely, higher NO_x (not shown) in run 5. This was associated with lower OH (3.9%, i.e., significant at the 99% confidence interval, Table 3) in run 5

OH (1.E4 molec/cc) run 4 (test sulfate) – run 3 (most comparable to other works)

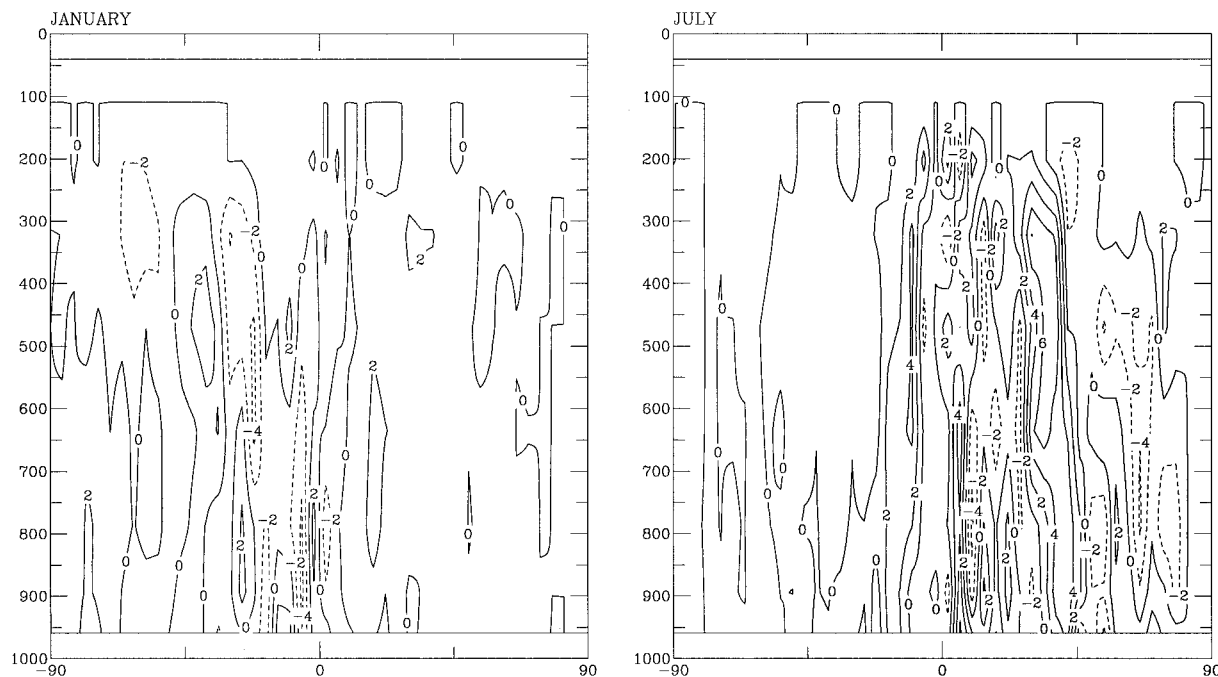


Figure 9. OH (1×10^4 molecules cm^{-3}) for run 4 (PI sulfate and emissions) – run 3 (PI emissions).

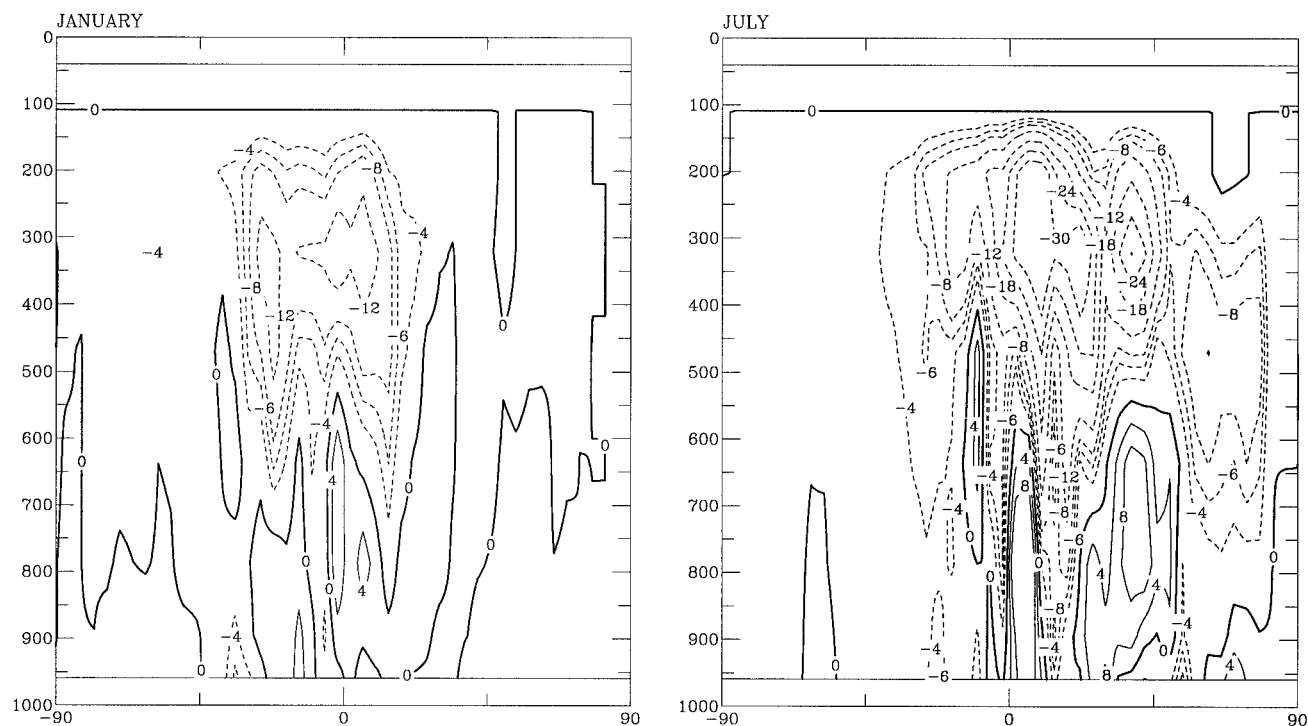
OH ($1.E4$ molec/cc) run 5 (test ocean) – run 4 (test sulfate)

Figure 10. OH (1×10^4 molecules cm^{-3}) for run 5 (PI sulfate, emissions, and ocean) – run 4 (PI sulfate and emissions).

(Figure 10), which was in turn associated with lower water levels (not shown) as a result of lower evaporative fluxes from the colder PI ocean.

Total tropospheric O_x burdens for run 5 (PI emissions, sulfate, and ocean) in Table 5 were 310 Tg corresponding to a 1.6% increase (of the order 95% significant in Table 3) on cooling the ocean. This arose despite a concomitant lowering in NO_x input from the lightning scheme from 3.86 (NH equal to 2.32, SH equal to 1.53) Tg N yr^{-1} to 3.62 (NH equal to 2.12, SH equal to 1.51). As already noted, our PI ocean run features lower H_2O , hence the $\text{O}^1\text{D} + \text{H}_2\text{O}$ sink is slowed which may account for the increase in PI O_x , at least in part. Consistent with this result, Fuglestad et al. [1995], Johnson et al. [1999], and Brasseur et al. [1998] predict a future decrease in ozone associated with a damper atmosphere leading to a faster $\text{O}^1\text{D} + \text{H}_2\text{O}$ sink. Grewe et al. [2001b], however, employed future (2015) SST data in the GISS model and found increased NO_x , hence ozone (of the order 10% in the tropics) which they attributed to changes in circulation, hence precipitation and washout. For the runs here, however, NO_x changes only very slightly when we cool the oceans (Table 2). Global mean OH values for run 5 were 10.3×10^5 molecules cm^{-3} (NH equal to 12.2, SH equal to 8.5) corresponding to a 3.9% (NH equal to 2.5, SH equal to 3.5) increase in changing from PI to PD ocean data (run 5 compared with run 4), which is significant to 99% (Table 3).

On plotting the change (%) in moist convective cloud cover due to cooling the ocean (Figure 11), run 5 (PI emissions, sulfate, and ocean) – run 4 (PI emissions and sulfate only) it was clear that the bulk of the cloud behavior noted in the best PI (section 3.1) run was attributable to changes in the ocean data. We now quantify this effect. Lower moisture fluxes from

the colder ocean leads to decreased tropical water vapor ($\sim 20\%$), decreased radiative heating hence decreased ($10\text{--}16 \times 10^5$ J m^{-2} sigma layer $^{-1}$) available potential energy (PE), slower ascent of the Hadley cell, and decreased convective cloud cover (e.g., by 2–4% in July in the tropics, $\sigma = 0.53\%$). Slowing the ascending Hadley cell also slows the adjacent, descending cells of dryer air, which leads to an increase in convective cloud cover in these regions, also in the range 2–4%.

Large increases in available PE ($30\text{--}40$ J m^{-2} sigma layer $^{-1}$) were also apparent over Antarctica during PI, possibly due to an enhanced ocean ice-albedo effect, although no corresponding increase in cloudiness was observed. This requires further investigation. Figure 12 shows changes in the mass stream function (MS) for run 5 (PI emissions, sulfate, and ocean) – run 4 (PI emissions and sulfate only). The MS is an indicator of the mean meridional circulation. Positive (negative) values indicate anticlockwise (clockwise) motion in the plane of the figure. In Figure 12, zonal mean rate of vertical overturn (10^9 kg s^{-1}) for the control run, $\text{MS}\sigma_{\text{global}} = 1.40, 0.97 \times 10^9$ kg s^{-1} in January, July, respectively, while at 550 mbar, $14\text{S MS } \sigma = 10.28, 6.47 \times 10^9$ kg s^{-1} for January, July, respectively. Figure 12 reveals decreased upward motion in the tropics and reduced downward transport of dry air in the subtropics, consistent with the cloud response. Corresponding features were noted in the input of NO_x by the interactive cloud-lightning scheme.

Inspecting the difference ($^{\circ}\text{C}$) in temperature for run 5 (PI emissions, sulfate, and ocean) – run 4 (PI emissions and sulfate only) (not shown) revealed that changing the ocean data accounted for the bulk of the temperature change in the best estimate PI run, i.e., results were almost identical to Figure 6, which showed temperature for control – run 2 (best PI). The

Moist convective clouds (%) run 5 – run 4

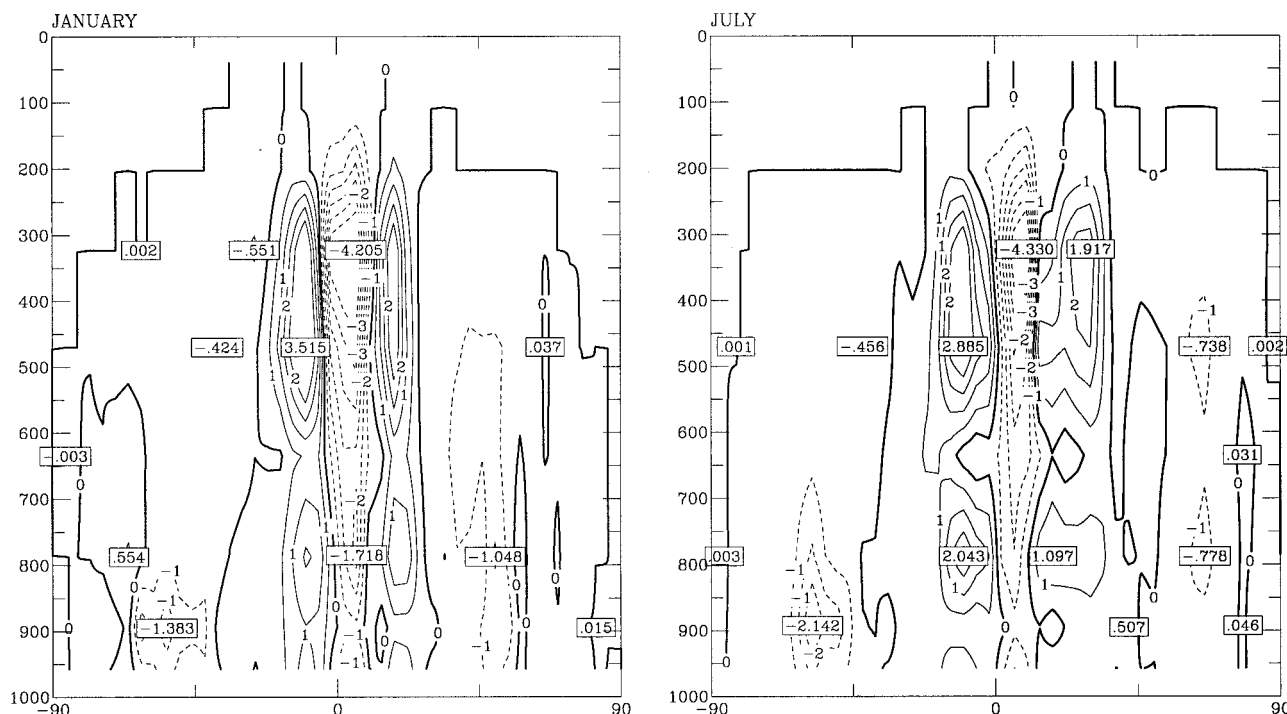


Figure 11. Moist convective cloud cover (%) for run 5 (PI sulfate, emissions, and ocean) – run 4 (PI sulfate and emissions).

drier PI troposphere is colder by 2° – 4°C over widespread regions, especially in the tropics around 300 mbar. The drier PI stratosphere warmed by around 1°C . Global mean temperature ($\sigma = 0.025^{\circ}\text{C}$) was higher by 1.629°C (NH equal to 1.359, SH equal to 1.900) for run 4 (PD ocean) compared with run 5 (PI ocean). (Here we quote global mean temperature to three decimal places because this order of accuracy is suggested by the standard deviation of model variability; we do not imply that the model reproduces this level of accuracy compared with observations.)

3.2.4. Effect of GHGs. On plotting the difference (ppbv) in O_x for run 2 (best PI estimate) – run 5 (all PI changes except GHGs), again we find small, anomalous higher PI O_x features (not shown) near the tropopause which are close to one standard deviation (Figure 3). Also, there exists a seasonal pattern over the pole at around 200 mbar with lower (higher) O_x in the summer (winter) for run 2 compared with run 5. Changes in NO_x (not shown) mostly explain the NH O_x behavior but not the SH. Figure 13 shows the difference (tenths $^{\circ}\text{C}$) in temperature (run 2 – run 5). There features weak (0.2° – 0.5°C) cooling during PI over wide areas in the troposphere, which may not be statistically significant (e.g., at 200 mbar in July is equal to 0.53°C). There is a possible, albeit weak, chemical contribution, namely, the reaction $\text{HO}_2 + \text{NO}$ which mediates in situ chemical ozone production and which shows a weakly negative temperature dependence, typical of many radical recombination reactions. Thus cooling is expected to lead to enhanced ozone via this process, although the weakness of the temperature dependence suggests ozone changes of only a couple of percent at most.

There also features PI cooling of up to 1° in high latitudes in the SH winter. Polar regions in the dark are sensitive to dy-

namical changes which affect poleward transport of heat. Lowering the GHGs led to a decrease in the rate of descent of the polar cell, consistent with the cooling feature. The phenomenon only features as a response to the GHGs being lowered; it is not evident, e.g., for the best estimate PI run.

The total tropospheric O_x burden for runs 5 and 2 (Table 5) were similar, corresponding to 310 and 306 Tg, respectively. O_x mixing ratios, however, tended to change most near the tropopause and may therefore impact the radiative calculations to a greater extent as will be discussed in section 3.3. Global mean OH values for run 5 and run 2 were also quite similar, corresponding to 10.3×10^5 molecules cm^{-3} (NH equal to 12.2, SH equal to 8.5) and 10.2×10^5 molecules cm^{-3} (NH equal to 12.0, SH equal to 8.4).

Global mean temperature increases were 0.153°C (NH equal to 0.231, SH equal to 0.076) for (run 5 – run 2), i.e. (PD GHGs – PI GHGs); $\sigma = 0.025^{\circ}\text{C}$. These values correspond only to reductions in the concentrations in air of the GHGs. They do not reflect feedbacks associated with ocean heating.

3.3. Radiative Feedbacks: Chemical Composition and Clouds

For any given, instantaneous forcing, the resulting response varies considerably between models. Over sufficiently long periods the response will feed back upon evolving chemical constituents such as ozone, and it will eventually impact future forcing values. Therefore radiative forcing (RF) definitions must also stipulate which, if any, model-dependent response(s) are included. The most common is that defined by IPCC [1996], which quotes RF at the tropopause after the stratosphere has been allowed to respond dynamically. Important quantities in our model which potentially feed back upon the

Mass stream function ($1.E9 \text{ kg/s}$) run 5 (test ocean) – run 4 (test sulfate)

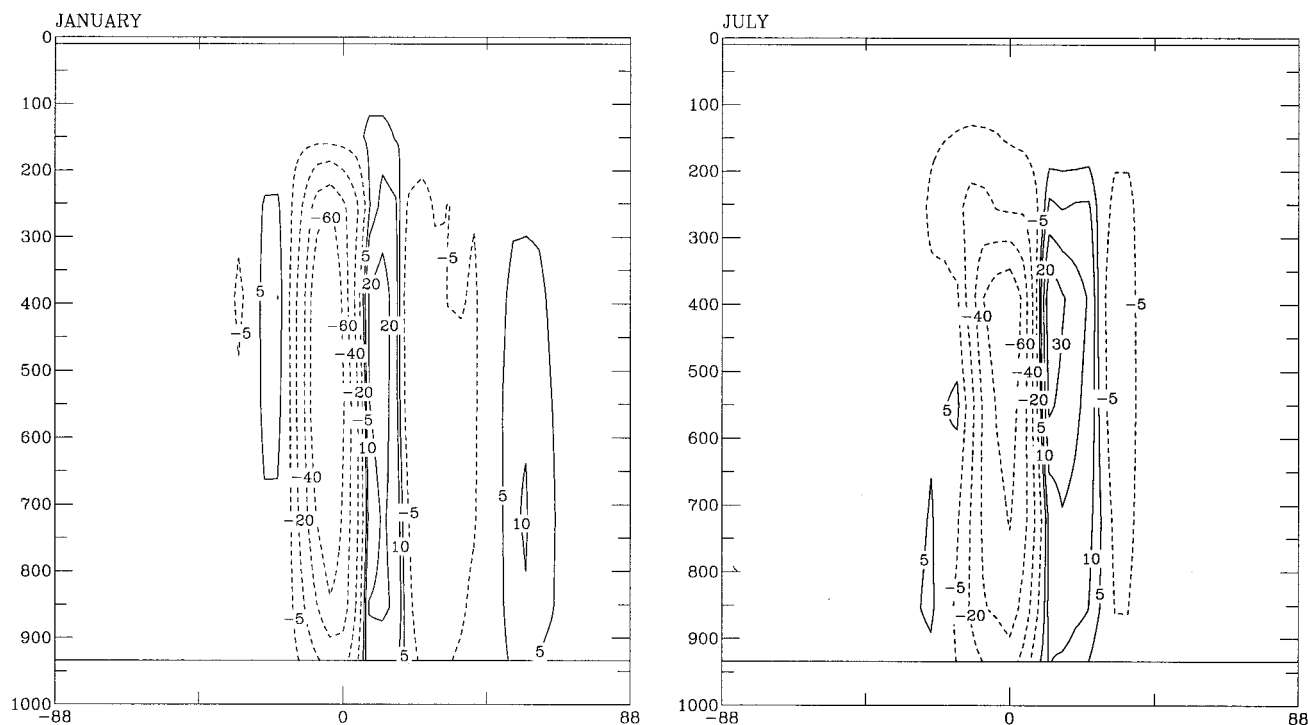


Figure 12. Mass stream function ($1 \times 10^9 \text{ kg s}^{-1}$) for run 5 (PI sulfate, emissions, and ocean) – run 4 (PI sulfate and emissions).

radiative forcing include dynamical, cloud, and albedo effects. Also, since we fix the SSTs, our model cannot fully respond over the longer oceanic timescales although we believe results are valid over the shorter (10 year) period employed. RF values as defined by IPCC [1996] are unavailable for the runs discussed here since the present calculations included the model-dependent response to ozone changes. However, future runs planned will calculate RF differences for PD and PI ozone distributions.

For run 3 (PI emissions) at NH midlatitudes ($\sim 500 \text{ mbar}$) we calculate a region of high ($40\text{--}50 \text{ ppbv}$) O_x (Figure 7) which lies directly above lower values. In the SH this does not occur, and there even is some indication of the reverse process taking place in the lower to midtroposphere at mid to high latitudes. Global mean RF increases due to enhanced tropospheric ozone occurring since PI is $0.4 (\pm 0.2) \text{ W m}^{-2}$. This is significant when compared with the same quantity summed for $(\text{CO}_2 + \text{CH}_4 + \text{N}_2\text{O}) = 2.5 (\pm 0.3) \text{ W m}^{-2}$ [IPCC, 1996]. Also, vertical (and horizontal) distributions of ozone tend to be less homogeneous compared with the other GHGs, due to its shorter lifetime. Introducing a heating source (O_x) high (low) in the troposphere such as the case in the NH (SH) tends to increase (decrease) atmospheric stability hence will decrease (increase) convective cloud cover (not shown) and so increase (decrease) SW absorption in the NH (SH). Models which employ climatological cloud cover will tend to overlook this phenomenon.

3.3.1. Sulfate aerosol. Sulfate aerosol as specified in the chemistry scheme may either increase or decrease NO_x (hence O_x) depending on location, as discussed in section 3.2.2. For the runs discussed here, the radiation scheme assumes a PD distribution of sulfate aerosol (as well as dust sea salt, organic

carbon, etc.) whose concentrations are slightly different from that used in the chemical calculations. The impact of this difference is likely to be small. Note that only sulfate in the chemistry subroutines was reduced to PI levels; the radiation sulfate was left unchanged. Globally, O_x and hence cloud responses were relatively small (2% decrease and 0.03–0.05% increase, respectively).

3.3.2. Ocean data. There featured relatively large responses in cloud cover to the PI ocean (Figure 11) which were different in sign between hemispheres (lower/higher in the NH/SH, respectively). Clouds were overall sparser in the NH because the large, central region of lowered cloudiness in Figure 11 was displaced across the equator toward the NH. PI ocean data led to lowered ($\sim 20\%$) water vapor in the tropics associated with slower Hadley overturning and increased atmospheric stability. There appears to exist radiative feedback between changes in radiative water, ocean ice, and cloudiness. Ozone values also changed near the tropopause, but a longer run is required to establish significance.

4. Conclusions

An important result is the cloud feedback mechanism. To the author's knowledge, other GCMs/CTMs which calculated O_x and OH changes since the PI era mostly employed climatological clouds and hence may produce different dynamical and cloud responses (which feed back upon the chemistry) compared with our runs which calculate cloud cover interactively. The contribution of clouds to the Earth's radiation budget is believed to fall generally within the range $20\text{--}60 \text{ W m}^{-2}$ for the LW heating component, with generally higher values associated with the SW cooling [Ramanathan, 1987] contribu-

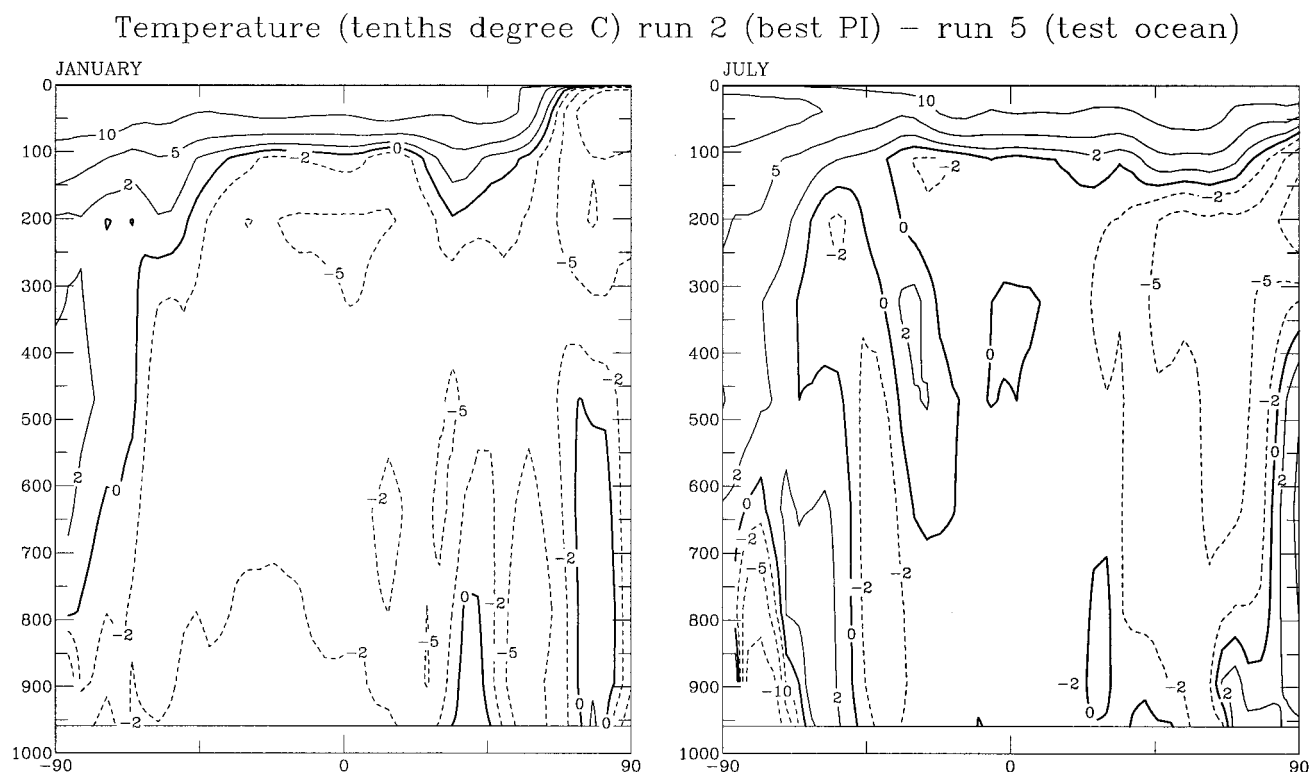


Figure 13. Temperature (tenths $^{\circ}\text{C}$) for run 2 (PI sulfate, emission, ocean, and GHGs) – run 5 (PI sulfate, emissions, ocean).

tion. Relatively small changes in global mean cloud cover therefore may produce radiative changes which are significant compared with the radiative changes associated with anthropogenic O_x increases which fall in the range $0.2\text{--}0.6\text{ W m}^{-2}$. Uncertainties associated with the cloud-radiation scheme and cloud feedback effects [Cess and Potter, 1987] are generally large in comparison. Changing the ocean data led to lowered H_2O and hence a slowing of the Hadley overturning which resulted in adjacent regions of depleted/enhanced tropical cloudiness in regions where upward/downward flow of moist/dry air are slowed. Therefore both the vertical position and magnitude of the change in GHGs play a role. This mechanism is also relevant for future predictive climate runs in which the vertical distributions of the GHGs H_2O and O_3 are expected to change. It is unclear whether future increases in ozone will occur mainly in the lower or upper troposphere. Also, other chemistry models currently used to predict future climate conditions are mainly CTMs which lack our cloud feedback mechanism [IPCC, 2001]. The mechanism may be sensitive to the vertical resolution. Earlier experiments with the GISS GCM using a finer vertical resolution and a higher model lid (23 layers, extending to 85 km) tended to magnify moist convective fluxes and increased release of latent heat in the troposphere [Rind and Lerner, 1996; Rind et al., 1998] which resulted in additional upper level cloud cover. This will tend to reinforce the conclusions of the present work. Cloud-chemistry interaction is an important area of future study. However, it is beyond the scope of the present paper to address this topic in full: in a forthcoming paper (J. L. Grenfell et al., manuscript in preparation, 2001) we include a complete analysis of cloud-ozone feedback. Compared to most other models, the GISS GCM possesses a generally simpler chemistry scheme yet a more

detailed cloud-radiation treatment. Despite this, our chemistry scheme has been found to compare favorably with other, generally more complex schemes. This paper and part 1 have shown that our calculated PD and PI O_x burdens compared well with other published works.

We also investigated the effect of lowering sulfate aerosol to PI conditions. Kiehl et al. [1999] also report lowering the sulfate burden, but it is unclear whether they did this uniformly or adopted a new PI distribution, as we did. Lowering sulfate in our model resulted in a succession of higher/lower NO_x (and O_x) features near the tropopause which require longer runs to establish whether they are significant or due to model variability. The overall effect on the O_x budget was small. However, since we do not include the effects of NMHCs, in situ ozone changes in our model are less sensitive to changes in NO_x arising from changes in sulfate.

On lowering only the precursor emissions, we obtained an ozone response similar to other works which lends confidence to our model results. Finally, we investigated the effect of lowering the GHGs. This strengthened the meridional temperature gradient and stimulated poleward transport of heat, resulting in extra heating of up to 1° in SH polar night. Understanding the changing face of chemistry-climate interaction remains a challenging problem.

Acknowledgments. The authors thank Richard Healy for providing preindustrial ocean data, Loretta Mickely for providing chemical emissions data, and Oliver Wild and Micheal Prather for providing the original “fastj” photolysis code. This work was funded under NASA’s Atmospheric Chemistry Modeling and Analysis Program under grant numbers NCC5-328 and EOS NCC 5-270.

References

- Baughcum, S. L., T. G. Tritz, S. C. Henderson, and D. C. Pickett, Scheduled civil aircraft emission inventories for 1992: Database development and analysis, *NASA Contract Rep.*, CR-4700, 1996.
- Bernsten, T. K., I. S. A. Isaksen, G. Myhre, J. S. Fuglestad, R. Stordal, T. A. Larsen, R. S. Freckleton, and K. P. Shine, Effects of anthropogenic emissions on tropospheric ozone and its radiative forcing, *J. Geophys. Res.*, **102**, 28,101–28,126, 1997.
- Brasseur, G. P., J. T. Kiehl, J. F. Müller, T. Schneider, C. Granier, X. Tie, and D. Hauglustaine, Past and future changes in global tropospheric ozone: Impact on radiative forcing, *Geophys. Res. Lett.*, **25**, 3807–3810, 1998.
- Cess, R. D., and G. L. Potter, Exploratory studies of cloud radiative forcing with a general circulation model, *Tellus, Ser. A*, **39**, 460–473, 1987.
- Chalita, S., D. A. Hauglustaine, H. Le Treut, and J. F. Mueller, Radiative forcing due to increased tropospheric ozone concentrations, *Atmos. Environ.*, **30**, 1641–1646, 1996.
- DeMore, W. B., S. P. Sander, C. J. Howard, A. R. Ravishankara, D. M. Golden, C. E. Kolb, R. F. Hampson, M. J. Molina, and M. J. Kurylo, Chemical kinetics and photochemical data for use in stratospheric modeling, *JPL Publ.*, 97-4, 1997.
- Dentener, F. J., and P. J. Crutzen, Reaction of N_2O_5 on tropospheric aerosols: Impact on the global distributions of NO_x , O_3 , and OH, *J. Geophys. Res.*, **98**, 7149–7163, 1993.
- Forster, P. M. F., C. E. Johnston, K. S. Law, J. A. Pyle, and K. P. Shine, Further estimates of radiative forcing due to tropospheric ozone changes, *Geophys. Res. Lett.*, **23**, 3321–3324, 1996.
- Fuglestad, J. S., J. E. Jonson, W. Wang, and I. S. A. Isaksen, Climate change and its effect on tropospheric ozone, in *Atmospheric Ozone as a Climate Gas*, edited by W. C. Wang and I. S. A. Isaksen, *NATO ASI Ser.*, **132**, 145–162, 1995.
- Grewe, V., D. Brunner, M. Dameris, J. L. Grenfell, R. Hein, D. Shindell, and J. Staehelin, Origin and variability of upper tropospheric nitrogen oxides and ozone at northern mid-latitudes, *Atmos. Environ., Part B*, **53**, 1–19, 2001a.
- Grewe, V., M. Dameris, R. Hein, R. Sausen, and B. Steil, Future changes in the atmospheric composition and the impact of climate change, *Tellus, Ser. B*, **53**, 103–121, 2001b.
- Hansen, J., G. Russell, D. Rind, P. Stone, A. Lacis, S. Lebedeff, R. Ruedy, and L. Travis, Efficient three-dimensional global models for climate studies: Models I and II, *Mon. Weather Rev.*, **111**, 609–662, 1983.
- Hansen, J., et al., Forcings and chaos in interannual to decadal climate change, *J. Geophys. Res.*, **102**, 25,679–25,720, 1997.
- Hauglustaine, D. A., C. Granier, G. P. Brasseur, and G. M. Mérieu, Importance of atmospheric chemistry in the calculation of radiative forcing on the climate system, *J. Geophys. Res.*, **99**, 1173–1186, 1994.
- Haywood, J. M., M. D. Schwarzkopf, and V. Ramaswamy, Estimates of radiative forcing due to modeled increases in tropospheric ozone, *J. Geophys. Res.*, **103**, 16,999–17,007, 1998.
- Intergovernmental Panel on Climate Change (IPCC), *Climate Change 1995: Contribution of Working Group I to the Second Assessment Report of the Intergovernmental Panel on Climate Change*, edited by J. T. Houghton et al., Cambridge Univ. Press, New York, 1996.
- Intergovernmental Panel on Climate Change (IPCC), *Climate Change: The Scientific Basis, Contribution of Working Group I to the Third Assessment Report of the Intergovernmental Panel on Climate Change*, edited by J. T. Houghton et al., 881 pp., Cambridge Univ. Press, New York, 2001.
- Johnson, C. E., W. J. Collins, D. S. Stevenson, and R. G. Derwent, Relative roles of climate and emissions changes on future oxidant concentrations, *J. Geophys. Res.*, **104**, 18,631–18,645, 1999.
- Kiehl, J. T., T. L. Schneider, R. W. Portmann, and S. Solomon, Climate forcing due to tropospheric and stratospheric ozone, *J. Geophys. Res.*, **104**, 31,239–31,254, 1999.
- Koch, D., D. Jacob, I. Tegen, D. Rind, and M. Chin, Tropospheric sulfur simulation and sulfate direct radiative forcing in the Goddard Institute for Space Studies general circulation model, *J. Geophys. Res.*, **104**, 23,799–23,822, 1999.
- Lelieveld, J., and R. van Dorland, Ox chemistry changes in the troposphere and consequent radiative forcing of climate, in *Atmospheric Ox as a Climate Gas*, edited by W. C. Wang and I. S. A. Isaksen, pp. 225–258, Springer-Verlag, New York, 1995.
- Levy, H., II, P. S. Kasibhata, W. J. Moxim, A. A. Klonecki, A. J. Hirsch, S. J. Oltmans, and W. L. Chameides, The global impact of human activity on tropospheric ozone, *Geophys. Res. Lett.*, **24**, 791–794, 1997.
- Mickley, L., P. P. Murti, D. J. Jacob, J. A. Logan, D. Koch, and D. Rind, Radiative forcing from tropospheric ozone calculated with a unified chemistry-climate model, *J. Geophys. Res.*, **104**, 30,153–30,172, 1999.
- Olson, J., et al., Results from the Intergovernmental Panel on Climate Change Photochemical Model Intercomparison (PhotoComp), *J. Geophys. Res.*, **102**, 5979–5991, 1997.
- Prather, M., Numerical advection by conservation of second-order moments, *J. Geophys. Res.*, **91**, 6671–6681, 1986.
- Price, C., J. Penner, and M. Prather, NO_x from lightning, 1, Global distribution based on lightning physics, *J. Geophys. Res.*, **102**, 5929–5941, 1997.
- Prinn, R. G., R. F. Weiss, B. R. Miller, J. Huang, F. N. Alyea, D. M. Cunnold, P. J. Fraser, D. E. Hartley, and P. G. Simmonds, Atmospheric trends and lifetime of CH_3CCl_3 and global OH concentrations, *Science*, **269**, 187–192, 1995.
- Ramanathan, V., Role of Earth radiation budget studies in climate and general circulation research, *J. Geophys. Res.*, **92**, 4075–4095, 1987.
- Rind, D., and J. Lerner, Use of on-line tracers as a diagnostic tool in GCM model development, *J. Geophys. Res.*, **101**, 12,667–12,683, 1996.
- Rind, D., D. Shindell, P. Lonergan, and N. K. Balachandran, Climate change and middle atmosphere, part III, The doubled CO_2 climate revisited, *J. Clim.*, **11**, 876–894, 1998.
- Roelofs, G. J., J. Lelieveld, and R. van Dorland, A three-dimensional chemistry/general circulation model simulation of anthropogenically derived ozone in the troposphere and its radiative forcing, *J. Geophys. Res.*, **102**, 23,389–23,401, 1997.
- Russell, G. L., J. R. Miller, and L. C. Tsang, Seasonal oceanic heat transports computed from an atmospheric model, *Dyn. Atmos. Oceans*, **9**, 253–271, 1985.
- Schulte, P., H. Schlager, H. Ziereis, U. Schumann, S. L. Baughcum, and F. Deidewig, NO_x emission indices of subsonic long-range jet aircraft at cruise altitude: In situ measurements and predictions, *J. Geophys. Res.*, **102**, 21,431–21,442, 1997.
- Shindell, D. T., J. L. Grenfell, D. Rind, C. Price, and V. Grewe, Chemistry-climate interactions in the Goddard Institute for Space Studies general circulation model, 1, Tropospheric chemistry, model description, and evaluation, *J. Geophys. Res.*, **106**, 8047–8076, 2001.
- Stevenson, D. S., C. E. Johnson, W. J. Collins, R. G. Derwent, and K. P. Shine, Evolution of tropospheric ozone radiative forcing, *Geophys. Res. Lett.*, **25**, 3819–3822, 1998.
- Van Dorland, R., F. J. Dentener, and J. Lelieveld, Radiative forcing due to tropospheric ozone and sulfate aerosols, *J. Geophys. Res.*, **102**, 28,079–28,100, 1997.
- Wang, Y., and D. J. Jacob, Anthropogenic forcing on tropospheric ozone and OH since preindustrial times, *J. Geophys. Res.*, **103**, 31,123–31,135, 1998.
- Wang, Y., D. J. Jacob, and J. A. Logan, Global simulation of tropospheric O_3 - NO_x -hydrocarbon chemistry, 1, Model formulation, *J. Geophys. Res.*, **103**, 10,713–10,725, 1998.

J. L. Grenfell, Stratosphärenguppe, Institut für Meteorologie, Freie Universität Berlin, Carl Heinrich Becker Weg 16, D-12165 Berlin, Germany. (grenfell@strat01.met.fu-berlin.de)
D. Koch, D. Rind, and D. T. Shindell, NASA Goddard Institute for Space Studies and Center for Climate Research, Columbia University, 2880 Broadway, New York, NY 10025, USA.

(Received October 26, 2000; revised June 29, 2001; accepted August 24, 2001.)

